Modified charge transfer–embedded atom method potential for metal/metal oxide systems

X. W. Zhou,[1,*] H. N. G. Wadley,[1] J.-S. Filhol,[2] and M. N. Neurock[2]
[1]*Department of Materials Science and Engineering, School of Engineering and Applied Science, University of Virginia, Charlottesville, Virginia 22903, USA*
[2]*Department of Chemical Engineering, School of Engineering and Applied Science, University of Virginia, Charlottesville, Virginia 22903, USA*
(Received 13 February 2003; revised manuscript received 25 August 2003; published 6 January 2004)

Atomistic simulations using interatomic potentials are widely used for analyzing phenomena as diverse as crystal growth and plastic deformation in all classes of materials. The potentials for some material classes, particularly those for metal oxides, are less satisfactory for certain simulations. Many of the potentials currently utilized for metal oxides incorporate a fixed charge ionic component to the interatomic binding. However, these fixed charge potentials incorrectly predict the cohesive energy of ionic materials, and they cannot be used to simulate oxidation at metal surfaces or analyze metal/oxide interfaces where the local ion charge can be significantly different from that in the bulk oxide. A recent charge transfer model proposed by Streitz and Mintmire has in part successfully addressed these issues. However, we find that this charge transfer model becomes unstable at small atomic spacings. As a result, it cannot be used for the studies of energetic processes such as ion bombardment (e.g., plasma-assisted vapor deposition) where some ions closely approach the others. Additionally, the Streitz-Mintmire charge transfer model cannot be applied to systems involving more than one metal element, precluding study of the oxidation of metal alloys and dissimilar metal oxide/metal oxide interfaces. We have analyzed the origin of these limitations and propose a modified charge transfer model to overcome them. We then unify metal alloy embedded atom method potentials and the modified form of the charge transfer potential to create a general potential that can be used to explore the oxidation of the metallic alloy and the energetic vapor deposition of oxides, and to probe the structure of dissimilar metal oxide/metal oxide or metal alloy/oxide multilayers. Numerical procedures have been developed to efficiently incorporate the potential in molecular dynamics simulations. Several case studies are presented to enable the potential fidelity to be assessed, and an example simulation of the vapor deposition of aluminum oxide is shown to illustrate the potential utility.

DOI: 10.1103/PhysRevB.69.035402 PACS number(s): 34.20.Cf, 61.50.Lt

I. INTRODUCTION

There are many technologically important uses of metal oxides and metal/metal oxide multilayers. For instance, the formation of aluminum oxide on aluminum or aluminum-rich alloys passivates the surface and kinetically inhibits its further oxidation, enabling aluminum's widespread use as an engineering material.[1] Metal oxides such as alumina (Al_2O_3) and zirconia (ZrO_2) are widely used as structural ceramics.[2,3] Yttria-stabilized zirconia deposited on alumina-forming alloys is widely used as a thermal protection system to significantly improve the life of hot-gas turbine engine components.[4] These thermal protection systems are one of the most critical technologies responsible for the ongoing performance improvements of aircraft engines. Metal oxides are also very widely used as dielectric insulators in electronics.[5] More recently, it has been found that a thin (<10 nm) aluminum oxide layer sandwiched between a pair of ferromagnetic metal layers can be used to construct a magnetic tunnel junction that can be used either as a magnetic sensor (for example, to read magnetically recorded data on a hard disk drive[6]) or as a magnetic random access memory.[7–11] The recent discovery of the TiO_2/Co ferromagnetic oxide semiconductor with Curie temperature above ambient[12] may extend the use of metal oxides to electron spin injection and spin filtering in future ''spintronic'' devices.[13]

The atomic scale structure and defects in bulk metal oxides and at the interfaces between different oxides or oxides and metals can significantly impact the performance of the materials and devices described above. Atomistic simulations in principle provide a way to study these structures and defects as well as the processes by which the oxides and oxide multilayers are synthesized either by vapor deposition or oxidation at a metal surface. These studies can reveal important insights into a variety of phenomena ranging from defect incorporation during synthesis to deformation during service. Such insights may help enhance many of the more recent and future applications of oxide-based materials and devices referred to above, provided some of the limitations of current interatomic potentials are overcome.

The structure of a metal oxide and its evolution during growth on a metal surface can be studied by several ''atomistic'' approaches. *Ab initio* or density-function calculations can be used to determine the energetics, crystal structures, lattice constants, elastic constants, and diffusion energy barriers. However, these quantum-mechanical calculations are currently too computationally expensive to explore the structures and morphologies that arise in the larger scale systems that contain more than 200 atoms. When accurate interatomic potentials are available, it is possible to simulate the structure of thousands or even millions of atoms using molecular dynamics (MD) and therefore to attack problems motivated by the technologies described above. Such potentials

also provide a convenient means to identify fundamental phenomena such as diffusion mechanisms and to calculate the energy barriers for mass transport either in the bulk or at the surface of a material.[14] This information can in turn be used in vary large scale Monte Carlo simulations of structure evolution.[15]

Numerous potentials have been proposed. The embedded atom method (EAM) potential originally proposed by Daw and Baskes[16] is a high-fidelity interatomic potential widely used for modeling metals (especially the fcc metals). This is because EAM captures the concept of metallic cohesion that arises from embedding ions in a gas of free electrons. A unified EAM potential database has recently been developed for 16 metals and their alloys.[17] Because the EAM potential captures many-body effects, the database has been successfully utilized to simulate atomic assembly mechanisms and to investigate the atomic structures of vapor deposited metals and metallic multilayers that exhibit giant magnetoresistance.[17,18]

A very rich interatomic potential literature is also available for the atomistic simulation of ionic systems. In these systems, a significant part of the interaction between the constituent atoms arises from the Coulomb force between cations and anions. Most ionic potentials have used a pairwise potential superimposed upon an electron shell model.[19–22] These potentials assume fixed charges on the cations and anions. In this limit, the pairwise potential, $\varphi_{ij}(r_{ij})$, between ionized atoms i and j separated by a distance r_{ij} can be written[22–24]

$$\varphi_{ij}(r_{ij}) = k_c \frac{q_i q_j}{r_{ij}} + A_{ij} \exp(-\nu_{ij} r_{ij}) - \frac{\zeta_{ij}}{r_{ij}^6}, \qquad (1)$$

where q_i and q_j are the charges on ions i and j, respectively, $k_c = 14.4$ eV Å e^{-2} is the Coulomb constant (e represents the electron charge), and A_{ij}, ν_{ij}, and ζ_{ij} are three free parameters that are determined by fitting to properties of the material system of interest. Typically, these consist of lattice constants, elastic constants, and cohesive energies.[23] In Eq. (1), the first term represents a long-range Coulomb interaction, the second term stands for a short-range repulsion, and the third term describes van der Waals attractions between charge clouds. For a fixed ion charge model, the charge on the ion is taken to be that of the valency of the atom, i.e., for aluminum, $q_{\mathrm{Al}} = 3e$; for zirconium, $q_{\mathrm{Zr}} = 4e$; and for oxygen, $q_{\mathrm{O}} = -2e$. Equation (1) can be easily implemented in efficient MD algorithms and has been widely used to study bulk oxides.[24,25] However, it has a number of shortcomings.

First, the fixed charge model does not allow the introduction of different oxidation states. Aluminum, for instance, can form different oxide compounds such as Al_2O_3 and AlO (or more generally, AlO_x) where the charge on the ions is a function of oxygen/aluminum ratio. If the charge utilized in a potential is fixed, it can only be used to study one oxidation state and cannot be used for a process such as oxidation in which the charge state varies. Furthermore, the fixed charge model cannot ensure charge neutrality for a simulated crystal if the cation and anion composition varies. The simulation of oxide vapor film deposition (which involves the random addition of cations and anions) can cause such unbalanced charges, which then affects the energetics of the entire computational system. As a result, simulations using such a model produce unrealistic results.

Second, the lattice energy calculated using a fixed charge potential corresponds to the energy required to separate a crystal into its individual (charged) ions so widely separated that they are no longer interacting. Such a charge ''cloud'' has a significant Coulomb energy. As a result, the lattice energy predicted by a fixed charge model is significantly higher than the experimentally measured cohesive energy, which is defined as the energy required to separate a crystal into individual neutral atoms. For cubic ZrO_2, the average lattice energy predicted by a fixed charge potential is around 30 eV/atom,[24] whereas the cohesive energy deduced from experimental data (see Appendix A) is only 7–8 eV/atom. This misrepresentation of cohesive energy results in wrong latent heat release during adatom condensation. Since a metal oxide is created from initially neutral atoms, an ideal ionic potential must allow the charge to decrease to zero as the ionically bonded crystal is pulled apart to create its constituent atoms.

A third problem with a fixed charge potential is that it cannot be used to study the structure of the interface between a metal and its oxide. The requirement here is that the potential switches between one dominated by ionic interactions in the oxide region to one dominated by metallic interactions in the metal region. The precise response will depend on the local (chemical) environment. A metal atom must have a zero charge when its neighbors are all metal atoms. It acquires a positive charge only when it gets close to negative charged oxygen atoms. A high positive charge is obtained when the metal surroundings have a high density of oxygen ions. Similarly, an oxygen atom should be neutral when it is embedded in an oxygen environment. It acquires negative charge only when it closely approaches positive charged metal atoms. A high negative charge results when its surroundings have a high density of metal ions. If an oxide crystal is cleaved, then the ions at unrelaxed surfaces have fewer neighbors of opposite charge but the bond length is the same as that in a bulk. As a result, charges on the ions should be able to decrease near unrelaxed surfaces.

A variable charge potential proposed by Streitz and Mintmire addressed these deficiencies.[26] This potential can be combined with an EAM potential so that ionic and metallic components of the interatomic interaction can both be incorporated.[26] However, as analyzed below, the Streitz-Mintmire potential becomes unstable for small ion spacings, and it lacks the generality to incorporate more than one metal element. The first problem has been found to impose serious constraints on the acceptable ranges for the EAM parameters needed to ensure stable simulations. The ensuing charge instability prevents the variable charge model from being combined with many existing EAM potentials, including the EAM potential database that successfully parameterized many metals and their alloys.[17] The second problem prevents the charge model from being used to simulate interfaces between different metal alloy oxides, or between metal alloy and metal alloy oxide.

Here, we explore these limitations and develop a modified charge transfer potential that overcomes the difficulties described above. We believe that the proposed potential is sufficiently general that it can be used to simulate the atomic scale structure of metal alloys, metal alloy oxides, and any mixtures of metal alloys and their oxides. As an implementation case study, we developed a specific potential for the O-Al-Zr system, and perform several simulations to assess the potential fidelity. We also show an example for applying the potential to simulate the vapor deposition of an alumina thin film.

II. CHARGE TRANSFER POTENTIALS

The newest variable charge potential was proposed by Streitz and Mintmire.[26] In their potential, the total energy of an ionic crystal, E_t, was divided into an electrostatic energy (E_{es}) that is ion charge dependent and a nonelectrostatic energy (E_n) that is ion charge independent:

$$E_t = E_{\mathrm{es}} + E_n . \tag{2}$$

If we normalize E_{es} so that it becomes zero when the ion charge is zero, E_n can be viewed as the energy of a nonionic crystal (e.g., a metal) and E_{es} then accounts for the electrostatic energy change as this crystal is ionized (e.g., by oxidation). Atomistic simulations require two separate models for calculating, respectively, E_{es} and E_n. In the Streitz-Mintmire formalism, E_n could not be represented by a pair potential because its integration with the E_{es} led to instabilities at metal oxide surfaces.[26] The modified E_{es} potential described below resolved this instability problem, and therefore any nonelectrostatic potential model can be used for E_n.

Since the ionic interactions and the charge transfer are only related to E_{es}, the E_{es} model is referred to as a charge transfer ionic potential (CTIP). For the convenience of discussion to follow, we summarize the Streitz-Mintmire CTIP model in Appendix B. To apply Eq. (B14) to calculate E_{es}, one needs to first calculate functions X_i and V_{ij} described in Appendix B by Eqs. (B12) and (B13) in terms of Coulomb integrals $[a|f_b]$ and $[f_a|f_b]$, where $a=i,j$, $b=i,j$, $a\neq b$. The expressions for $[a|f_b]$ and $[f_a|f_b]$ are not trivial to deduce. As a result, we list our derived equations for $[a|f_b]$ and $[f_a|f_b]$ here:

$$[a|f_b] = \frac{1}{r_{ab}} - \xi_b \exp(-2\xi_b r_{ab}) - \frac{1}{r_{ab}} \exp(-2\xi_b r_{ab}), \tag{3}$$

for $\xi_a = \xi_b = \xi$,

$$[f_a|f_b] = \frac{1}{r_{ab}} [1 - (1 + \tfrac{11}{8}\xi r_{ab} + \tfrac{3}{4}\xi^2 r_{ab}^2 + \tfrac{1}{6}\xi^3 r_{ab}^3) \times \exp(-2\xi r_{ab})], \tag{4}$$

and for $\xi_a \neq \xi_b$,

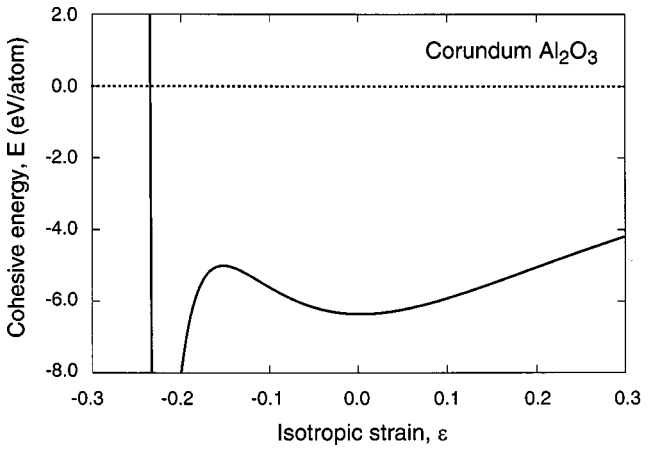

FIG. 1. Cohesive energy of corundum Al_2O_3 as a function of isotropic strain predicted by the old charge transfer model.

$$[f_a|f_b] = \frac{1}{r_{ab}} - \frac{\xi_a \xi_b^4 \exp(-2\xi_a r_{ab})}{(\xi_a+\xi_b)^2(\xi_a-\xi_b)^2} - \frac{\xi_b \xi_a^4 \exp(-2\xi_b r_{ab})}{(\xi_b+\xi_a)^2(\xi_b-\xi_a)^2} - \frac{(3\xi_a^2\xi_b^4 - \xi_b^6)\exp(-2\xi_a r_{ab})}{r_{ab}(\xi_a+\xi_b)^3(\xi_a-\xi_b)^3} - \frac{(3\xi_b^2\xi_a^4 - \xi_a^6)\exp(-2\xi_b r_{ab})}{r_{ab}(\xi_b+\xi_a)^3(\xi_b-\xi_a)^3}. \tag{5}$$

It should be pointed out that V_{ij} involves a summation of $\Sigma_{k=j(i_1)}^{j(i_N)} k_c [f_i|f_k]$ [see Eq. (B13)]. According to Eqs. (4) and (5), V_{ij} includes a summation of $\Sigma_{k=j(i_1)}^{j(i_N)} k_c / r_{ik}$. The direct summation of the slowly decaying $1/r_{ik}$ function imposes a serious divergence problem. The Ewald summation technique as described in Appendix C is therefore used to calculate V_{ij}.

The Streitz-Mintmire CTIP model has been combined with an embedded atom method potential for nonelectrostatic interactions and used to simulate the binary aluminum-oxygen system.[26] Using this Al-O potential, our simulations of Al/AlO_x multilayers correctly predicted zero charge in the bulk aluminum, a maximum cation and anion charge in the bulk oxide, and a partial cation and anion charge near the Al/AlO_x interface. It also correctly predicted the charge decrease near an oxide surface.[26] This Al-O potential has allowed a successful simulation of the dynamics of oxide scale formation on aluminum surfaces.[27,28]

However, we found that the potential has two problems. To illustrate the first, we calculated the cohesive energy of the α (corundum) phase of Al_2O_3 over a wide range of lattice constants using the original potential.[26] The results are plotted in Fig. 1 as a function of isotropic strain defined as $\varepsilon = (a - a_0)/a_0$, where a_0 represents the equilibrium lattice constant and a is the lattice constant after a hydrostatic volume change. Figure 1 indicates that the charge transfer model reasonably predicts a local energy minimum at the equilibrium (nonstrained) crystal lattice length. However, the cohesive energy versus strain relation has a local maximum

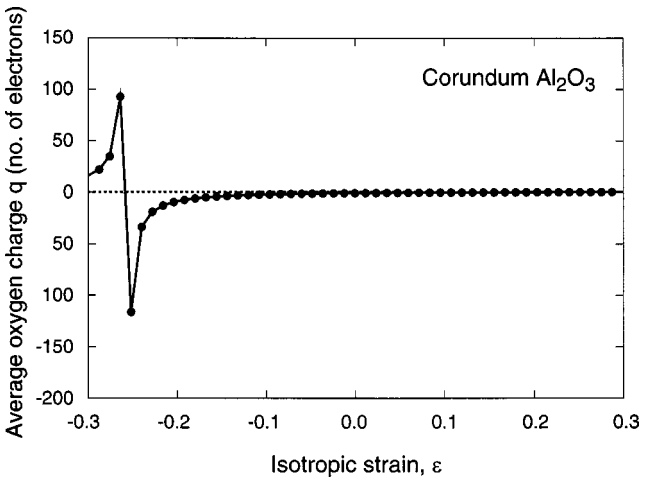

FIG. 2. Average anion charge of corundum Al_2O_3 as a function of isotropic strain predicted by the old charge transfer model.

as the crystal is compressed beyond a strain of about -0.16 and becomes unstable when the crystal is further compressed beyond a strain of about -0.23.

To investigate the origin of this effect, we calculated the charge on each ion as a function of crystal size. The average oxygen ion charge is plotted in Fig. 2 as a function of the isotropic strain. It can be seen that the magnitude of the charge asymptotically decreases towards near-zero as the crystal is expanded. It becomes increasingly negative as crystal is slightly compressed. However, when the crystal is compressed below a strain of -0.2, the charge becomes unstable and oscillates between large physically unrealistic values.

To understand the origin of the charge instability, we need to consider only a simplified system containing a cation and an anion pair, with each assumed to be a point charge. According to Eqs. (B1)–(B3) and (B14), the electrostatic energy for such a pair can be written as

$$E_{\mathrm{es}}=\chi_1 q_1+\tfrac{1}{2}J_1 q_1^2+\chi_2 q_2+\tfrac{1}{2}J_2 q_2^2+k_c\frac{q_1 q_2}{r_{12}}. \qquad (6)$$

If the overall system is charge neutral, $q_1=-q_2$. Equation (6) then becomes

$$E_{\mathrm{es}}=(\chi_1-\chi_2)q_1+\left(\frac{J_1+J_2}{2}-\frac{k_c}{r_{12}}\right)q_1^2. \qquad (7)$$

Equation (7) only has a well-defined minimum when $(J_1+J_2)/2-k_c/r_{12}>0$ (i.e., a concave parabolic curve). However, for a set of model parameters (J_1 and J_2) that are prescribed to satisfy this condition at the initial r_{12}, there is always a critical value for a reduced r_{12} below which $(J_1+J_2)/2-k_c/r_{12}<0$. This corresponds to the condition where the Coulomb interaction between the neighboring cation and anion overpowers the other energy terms. When this happens, Eq. (7) ceases to have a minimum (it becomes a convex parabolic curve), and E_{es} always reduces as the magnitude of charge increases. The problem is serious for variable charge models because as the magnitude of the charges of neighboring cation and anion increases to reduce E_{es}, the increased attraction drives the two ions closer. This promotes a further increase in the magnitude of the charges. Repetition of this process results either in calculation overflow (most likely) or unrealistic results. It should be noted that for a system containing many atoms, the problem can be triggered when any pair of ions becomes close.

In spite of the instability shown in Fig. 1, the original model and the proposed potential parameters[26] have been satisfactorily used in a number of different simulations.[26–28] This is because the nonelectrostatic parameters defining the short-range repulsion between atoms have been constructed to prevent atoms from getting too close (thus, the unstable charge crystal configurations such as the highly compressed one shown in Figs. 1 and 2 do not occur) in the simulations. However, the instability is still a very serious problem for the original CTIP model. This is because while Fig. 1 shows the occurrence of the problem when a bulk ionic system is highly compressed (to below -0.2), the same problem could occur in much less compressed systems that contain nonbulk configurations such as free surfaces and interfaces. It may also occur when a surface is impacted by energetic atoms or ions. In these cases, the local interaction difference or the impact can cause an atom or ion to closely approach another atom or ion. We have also found that the original CTIP model[26] is always unstable and always causes calculation overflow if it is combined with other EAM potentials such as that reported in Ref. 17 to even simulate an uncompressed ZrO_2 or AlO_2 surface. In addition, we have discovered that the overflow encountered during efforts to use the pair potential to approximate E_n (Ref. 26) also resulted from this instability. The constraint that the original CTIP model imposes on the choice of the nonelectrostatic potential (including both format and parameters) is clearly nonphysical and prevents a merging of the CTIP with the existing metal alloy EAM potential database for a variety of metals.

The second problem with the original charge transfer model is that it can only be used to study oxygen–single-metal (binary) systems. Our underlying objective is to superimpose a CTIP potential with an EAM potential so that the integrated CTIP+EAM potential can be simultaneously applicable to pure metals, pure oxygen, and to the mixtures of different oxides and different metals. The total energy of the EAM model, represented here by the nonelectrostatic energy E_n has been established to fully describe metal alloy systems.[17] In order for the integrated CTIP+EAM potential to be invariant against the EAM potential of metals, the total energy of the CTIP+EAM potential, $E_t=E_{\mathrm{es}}+E_n$, must be reduced to $E_t=E_n$ in pure metal alloy systems. This requires that $E_{\mathrm{es}}=0$ for all metal alloy systems. Equation (B14) indicates that the normalized electrostatic potential E_{es} vanishes when all the charges q_i become zero. This means that the CTIP model must predict zero charges in pure metal alloy systems. Note here that metal alloys can have minor charges from first principles. This charge contribution, however, has been implicitly included in the EAM and the zero charge assumption is in fact mandatory to comply with the notion that the EAM fully describes metal systems.

The Streitz-Mintmire original CTIP model correctly predicts zero charge for aluminum atoms in either bulk aluminum or a local aluminum region of the Al/AlO_x multilayers. However, this is achieved only when a single metal is involved and nonzero charge will be obtained in any metal alloy systems. To illustrate, consider again a simple pair of point charges. Setting the first derivative of the electrostatic energy [Eq. (7)] with respect to q_1 equal to zero yields

$$q_1 = \frac{\chi_2 - \chi_1}{J_1 + J_2 - 2k_c/r_{12}}. \tag{8}$$

It is seen that q_1 is zero only when χ_1 and χ_2 are identical (i.e., 1 and 2 are of the same species). In a single-metal region, all atoms have the same charge properties. As a result, no atoms can have a preference to become a positive charge by inducing negative charges to its neighbors, and zero charge is naturally achieved. In metal alloys, however, neighboring atoms can be different metal species. They therefore will have different charge parameters. As a result, the original CTIP model will predict nonzero charges for a pure (unoxidized) metal alloy region. If this happens, the integrated CTIP+EAM potential will be different from the EAM potential for pure metal systems. A physical method to ensure zero charge in any metal alloy needs to be developed in order for the model to be used in systems that include more than one metal elements.

III. CTIP MODIFICATIONS

The discussions above clearly indicate that simulations based upon the old CTIP model are unstable when configurations with small lattice spacings are encountered. In this regime, the electrostatic energy is dominated by Coulomb interactions. When this occurs, the system energy continuously decreases as the magnitude of the charge on the neighboring cation and anion increases. Energy minimization then leads to unrealistically large charges. In reality, the charge on an ion is always bounded. For instance, the maximum charge of a cation is usually limited by the number of valence electrons as much higher energies are required to extract inner-shell electrons. Obviously, a physical CTIP-type model must ensure reasonable charge bounds for each ion. It should be pointed out that unlimited charge is directly responsible for the observed divergence. For instance, when negative charge and positive charge start to interact, they tend to increase their magnitudes of charge (due to energy minimization). This will increase the attraction between them and cause them to become closer. This in turn promotes further increases in charge. If the charges are not bounded, the continuous increase of the attraction due to increases in charge during this process can cause atoms to become infinitely close and a divergence occurs. As a result, while imposing charge bounds does not directly change the Coulomb equation at small atomic distances, it effectively eliminated the instability problem.

To extend a CTIP model to metal alloy oxidation, the key is to predict zero charges for the unoxidized metal alloy and significant charges for metal oxides. It should be pointed out that in the original CTIP model, the oxygen and the metal were distinguished only by their charge parameters. As Eq. (8) has indicated, the only driving force to induce charges in this model is the relative difference of the charge parameters between the neighboring atoms. When the charge parameters are prescribed, the charges are defined regardless of the species (oxygen or metal) of the neighboring atoms. The difficulty is that different metal species always have different charge parameters. The problem is compounded because the difference of the charge parameters between some metals may even be more significant than that between oxygen and some of the metals. To ensure zero charges in unoxidized metals and significant charges in oxidized metals is then a challenging task. Obviously, the potential must also distinguish between metal and oxygen atoms by something other than their charge parameters.

As discussed above, charge bounds can be used to solve the instability problem of the original CTIP model. The same approach can also be used to ensure zero charges for unoxidized metal alloys. Because metal atoms are assumed to be cations and oxygen atoms are assumed to be anions, it is then reasonable to bound the charge of each metal atom to q_M, such that $0 \leqslant q_M \leqslant q_{\max,M}$, and to bound the charge of each oxygen atom to q_O, such that $q_{\min,O} \leqslant q_M \leqslant 0$. The potential then naturally distinguishes metal and oxygen atoms by the sign of their charge bound. This guarantees zero charge in unoxidized metal alloy regions.

To illustrate, consider an aluminum and zirconium atom pair. Let us assume that the zirconium atom wants to become positively charged by inducing a negative charge on the aluminum atom. The aluminum atom, however, cannot become negatively charged because it is set to be in the positive charge range. This would force the aluminum charge to become zero. Zirconium, on the other hand, cannot stay positively charged because it does not have anions to interact with. Note in this simple case of a dimer, the system neutrality requirement also forces the charges to be zero. Since zero charges are guaranteed, the full CTIP+EAM model is invariant against the EAM potential, providing a basis for the general combination of an alloy EAM database with a CTIP model.

This simple approach captures the essential physics during charge transfer, i.e., metal atoms only lose electrons until all their valence electrons are gone, while oxygen atoms only acquire electrons until their outer electron shells are filled. It is the implementation of this physics that solves both problems of the original CTIP model.

While the physical underpinnings of this idea are simple, a modestly elaborate methodology is required to apply it. To overcome the difficulties in enforcing the charge bounds, we added two additional terms to the electrostatic energy, Eq. (B14). To maintain the integrity of the Streitz-Mintmire model, it is required that the additional terms become exactly equal to zero when the ion charges are within their chosen bounds. To prevent charges from far exceeding the bounds, the additional energy terms increase rapidly as the charges exceed the bound values. Such terms can be simply written as

$$E_{\mathrm{es}}=\sum_{i=1}^{N} q_i\chi_i+\tfrac{1}{2}\sum_{i=1}^{N}\sum_{j=1}^{N} q_iq_jV_{ij}+\sum_{i=1}^{N}\omega\left(1-\frac{q_i-q_{\min,i}}{|q_i-q_{\min,i}|}\right)\times(q_i-q_{\min,i})^2+\sum_{i=1}^{N}\omega\left(1-\frac{q_{\max,i}-q_i}{|q_i-q_{\max,i}|}\right)(q_i-q_{\max,i})^2, \tag{9}$$

where $q_{\min,i}$ and $q_{\max,i}$ are the bounds for the charge of atom i, $q_{\min,i}<q_i<q_{\max,i}$, and the coefficient ω can control how strongly the charge is confined by the bounds (physically this also corresponds to the energy penalty for metal atoms to obtain electrons or to lose inner-shell electrons or for oxygen atoms to lose electrons or to receive more than two electrons).

Using the simple case of a cation and anion pair, it can be proven that Eq. (9) significantly stabilizes the calculation. Assuming that the anion charge q_1 and the cation charge q_2 both seek to exceed the intended charge bounds, Eq. (7) can be rewritten with the modified model as

$$E_{\mathrm{es}}=[\chi_1-\chi_2+4\omega(q_{\max,2}-q_{\min,1})]q_1+\left(\frac{J_1+J_2}{2}-\frac{k_c}{r_{12}}+4\omega\right)q_1^2+2\omega(q_{\min,1}^2+q_{\max,2}^2). \tag{10}$$

Using the Streitz and Mintmire data ($J_1=14.04$ eV, $J_2=10.33$ eV), the separation distance below which divergence occurs for a dimer is approximately $r_{12}=2k_c/(J_1+J_2)=1.2$ Å in the Streitz-Mintmire old model [Eq. (7)]. Using the new model, Eq. (10), and a value of $\omega=20.0$, this divergence separation is significantly reduced to $r_{12}=2k_c/(J_1+J_2+8\omega)=0.156$ Å. Most importantly, the modified model allows J_1 and J_2 to be freely fitted to physical values without any constraints because even when J_1 and J_2 are both zero, Eq. (10) still predicts a very small divergence radius $r_{12}=2k_c/8\omega=0.18$ Å, whereas the earlier model predicts $r_{12}=\infty$.

Equation (9) must be numerically solvable for this model to be successful. In order for Eq. (9) to possess a well-defined minimum, it must be continuous and have continuous first derivatives. The prefactors before the $(q_i-q_{\min,i})^2$ and $(q_i-q_{\max,i})^2$ terms abruptly change from 0 to 2ω at their respective junctions $q_{\min,i}$ and $q_{\max,i}$. However, because both $(q_i-q_{\min,i})^2$ and $(q_i-q_{\max,i})^2$ and their first derivatives diminish at the junctions, the added terms are still continuous and have continuous first derivatives.

The modified equation (9) remains quadratic in nature. Unlike the quadratic function, Eq. (B14), some prefactors in Eq. (9) are not constant (step functions). As a result, $\partial E_{\mathrm{eq}}/\partial q_i=0$ will not be the "normal" system of linear equations. Equations (B16) and (B17) can no longer be used to solve for the charges. On the other hand, solving charges by a matrix operation is not efficient, especially when the number of atoms is large. An alternative computationally efficient algorithm was therefore sought.

Using $\Sigma_{i=1}^{N}q_i=0$, Eq. (9) is a function of $N-1$ independent variables $q_1,q_2,\ldots,q_{N-1}$. Appendix D illustrates that an integrated conjugate gradient technique combined with a Newton-Raphson method can be used to minimize this function containing nonconstant coefficients. Since the function to be minimized is essentially quadratic, the conjugate gradient method guarantees the convergence to the charge solutions that can provide accurate calculations for energy, forces, and stresses. This was also found to be much more computationally efficient than the matrix operations using Eqs. (B16) and (B17).

IV. MODIFIED EMBEDDED ATOM METHOD

Pair potentials can, of course, be used for the nonelectrostatic interactions E_n. Since the intent here is to extend the approach to study the oxidation of a variety of metals, we seek to apply an existing good metallic potential database to approximate E_n. The EAM potentials initially developed by Daw and Baskes[16] improve over the pair potentials by incorporating environment dependence of the atomic interactions. The existing EAM metallic potential database[17] has been successfully utilized to simulate a variety of metal problems, especially the atomic assembly mechanisms and atomic structures of vapor-deposited metals and metallic multilayers.[17,18] The EAM database[17] is hence chosen for our work. The EAM database model is described in Appendix E.

Since our improved CTIP model has zero effect on the calculation of the metal systems, the existing metal EAM potential parameters[17] and Eqs. (E1)–(E8) can in principle be used directly. However, it is useful to notice that the normalized embedding energy functions, Eqs. (E5)–(E7), are expressed in terms of relative electron density. As a result, only the ratios (not the absolute values) of f_e, ρ_e, and ρ_s affect the predicted properties of elemental metals. This feature can be utilized to fine-tune the properties of alloys and oxides. As a result, we adjust the parameters f_e, ρ_e and ρ_s in the EAM database[17] by a scaling factor g (i.e., $f_eg\rightarrow f_e$, $\rho_eg\rightarrow\rho_e$, and $\rho_sg\rightarrow\rho_s$, with g being the only adjustable parameter) to fit to the corresponding oxide's properties. Once the g factor is given, the metal potentials are completely defined by the existing EAM database.[17] Then, we need only determine the pair potential between oxygen atoms, the various pair potentials between oxygen and the various metal atoms, the electron density of oxygen, the embedding energy of oxygen, and the g factors for the different metal species. These can be defined by fitting model predictions to the known properties of oxides. To avoid the additional complexity due to different interactions between O_2 molecules and between the two oxygen atoms within an O_2 molecule, we assumed that oxygen takes the atomic form rather than a diatomic molecule. While this is an approximation, the interaction between a solid surface and O_2 gas can still be conducted in MD by introducing oxygen dimers rather than atomic oxygen on the surface. This is a sensible approach for the simple potential being sought. Note that the experimental cohesive energy of metal oxides implicitly includes the cohesive energy of the diatomic oxygen molecule (see Appendix A).

Equation (E3) is a universal format for pair potentials. We find that the pair potential between oxygen atoms can be well

fitted by Eq. (E3). Efforts have been made to use the alloy formula, Eq. (E8), to approximate the cross pair potentials between oxygen and metal atoms so that no additional fitting is required once the elemental potentials are known. However, the results have not been satisfactory. It was realized that the oxygen crystal has a lower melting temperature and therefore a lower cohesive energy than the metals. On the other hand, metal oxides usually have larger cohesive energies than metals. The extra cohesive energies of the oxides must therefore come from a stronger interaction between oxygen and metal atoms. The Coulomb interaction predicted by the CTIP model cannot alone provide this stronger interaction. The covalent nature of this interaction must therefore be included in the pair potentials. It cannot be approximated by Eq. (E8), which is essentially the weighted average of the oxygen-oxygen and metal-metal pair potentials. We therefore independently fit each oxygen-metal pair potential using Eq. (E3).

The electron density of oxygen was fitted using Eq. (11). Unlike Eq. (E4) where β and λ are the same as those in the attractive part in the pair potential, we introduce here new fitting parameters Γ and Ψ to provide more freedom for a better fit to the oxide properties:

$$f(r)=\frac{f_e \exp[-\Gamma(r/r_e-1)]}{1+(r/r_e-\Psi)^{20}}. \tag{11}$$

The present model is intended to be applicable for systems with oxygen and an arbitrary number (M) of metal elements. At least M different binary oxides involving the M metal elements need to be simultaneously fitted to get the cross pair potentials between oxygen and these metals. If we want to fit M binary oxides, there will be M nonequivalent oxygen lattice sites in these M oxides. These M sites correspond to M equilibrium electron densities, $\rho_{e,i}$, where $i=1,2,...,M$. An oxygen embedding energy function must sequentially go through these electron densities as the electron density increases. For the convenience of discussion, we can arrange the M oxides so that $\rho_{e,1},\rho_{e,2},\ldots,\rho_{e,M}$, refers to an increasing sequence of the electron densities.

The most straightforward way to fit an oxygen embedding energy function that smoothly goes through these electron densities is to use the spline functions. To fit the cohesive energy, the lattice constant, and bulk modulus of an oxide i exactly, the oxygen embedding energy and its first and second derivatives need to be exact, at least within a small electron density range near $\rho_{e,i},\rho_{\min,i}\leqslant\rho<\rho_{\max,i}$, where $\rho_{\min,i}<\rho_{e,i}$, and $\rho_{\max,i}>\rho_{e,i}$. A quadratic function can be used to achieve this. For M oxides, we then obtain an M number of oxygen embedding energy functions:

$$F_{0,i}(\rho)=\sum_{n=0}^{2} F_{n,i}\left(\frac{\rho}{\rho_{e,i}}-1\right)^n, \quad \rho_{\min,i}\leqslant\rho<\rho_{\max,i}, \quad i=1,2,...,M. \tag{12}$$

For an oxygen embedding energy function to be continuous, $\rho_{\min,i}$ and $\rho_{\max,i}$ can be simply set as $\rho_{\min,i}=0.5(\rho_{e,i-1}+\rho_{e,i})$, and $\rho_{\max,i}=0.5(\rho_{e,i}+\rho_{e,i+1})$, where only $\rho_{\min,1}$ and $\rho_{\max,M}$ are not defined. We then take $\rho_{\min,1}$ as $0.85\rho_{e,1}$, and $\rho_{\max,M}$ as ∞. The only undefined embedding energy function is in the $0-\rho_{\min,1}$ range. We can again use a polynomial function as shown in Eq. (13) to fit this range, where a higher power ($n=3$) term is introduced so the function can be fitted under the physical condition of $F_{0,0}=0$ at $\rho=0$. With these function formats given, the fitting was designed to result in smooth values and first derivatives for the oxygen embedding energy function at the spline junctions:

$$F_{0,0}(\rho)=\sum_{n=0}^{3} F_{n,0}\left(\frac{\rho}{\rho_{e,0}}-1\right)^n, \quad \rho<\rho_{\min,1}, \quad \rho_{e,0}=\rho_{\min,1}. \tag{13}$$

V. PARAMETRIZATION

To accurately account for the Coulomb interactions, a relatively long cutoff distance of 12 Å was used. Although it

TABLE I. EAM parameters for metals.

Metal	r_e (Å)	f_e	ρ_e	ρ_s	α
Al	2.863 924	1.343 867	19.556 03	22.216 28	6.613 165
Zr	3.199 978	1.591 439	22.028 52	22.028 52	8.559 190
	β	A (eV)	B (eV)	κ	λ
Al	3.527 021	0.314 873	0.365 551	0.379 846	0.759 692
Zr	4.564 902	0.424 667	0.640 054	0.5	1.0
	F_{n0} (eV)	F_{n1} (eV)	F_{n2} (eV)	F_{n3} (eV)	F_0 (eV)
Al	−2.807 602	−0.301 435	1.258 562	−1.247 604	−2.83
Zr	−4.485 793	−0.293 128	0.990 145	−3.202 519	−4.51
	F_1 (eV)	F_2 (eV)	F_3 (eV)	η	F_e (eV)
Al	0.0	0.622 245	−2.488 244	0.785 910	−2.824 528
Zr	0.0	0.928 602	−0.981 870	0.597 001	−4.509 017

TABLE II. Model predicted and target properties of fcc aluminum and hcp zirconium.

Physical property		Al		Zr	
		Predicted	Target	Predicted	Target
Lattice constants (Å)	a	4.050	4.050	3.202	3.202
	c			5.229	5.229
E_c (eV)		3.580	3.580	6.360	6.360
Bulk modulus (eV/Å^3)	B	0.474	0.474	0.606	0.604
Shear modulus (eV/Å^3)	G	0.164	0.164	0.228	0.230
anisotropy ratio	A	0.819	0.820	1.384	

is possible to use a second shorter cutoff distance for the nonelectrostatic EAM interactions to improve calculation efficiency, for simplicity no such efforts were made here.

The CTIP+EAM model retains the invariance of the EAM for pure metal systems. Based on this, the same metal EAM parameters as those published[17] could be used. Nevertheless, since the publication of the EAM database,[17] we have slightly modified some of the parameters in light of additional studies. The modified set of the parameters is shown in Table I. Because the EAM format allows the potential to be naturally cut off at around the fifth nearest neighbor (Appendix E), the extension of the cutoff distance does not affect the results of the EAM calculations. These EAM potentials for elemental cubic metals have already been well fitted to the lattice constant, cohesive energy, bulk modulus, shear modulus, anisotropic ratio, and the pressure derivative of the bulk modulus.[17] A comparison between predicted properties and target properties is shown in Table II.

In Table II, the target values of lattice constant, cohesive energy, and elastic constants are all experimental data.[17] The anisotropy ratio of hcp Zr have not been specifically fitted.[17] It can be seen that by using the EAM parameters of Table I, the experimental properties of the pure metals can be well predicted.

Potential parameters that give rise to good predictions of the properties of both aluminum oxides and zirconium oxides are needed. The corundum phase of Al_2O_3 is a stable structure at both low and high temperatures, and hence it was the natural choice for the parametrization. ZrO_2 has several different crystal structure forms. It exhibits a monoclinic structure at low temperatures, a tetragonal structure at intermediate temperatures, and a cubic structure at high temperatures. Since many zirconia materials are either manufactured or applied at high temperatures, the cubic ZrO_2 structure was used for deriving the potentials described below. A similar approach can also be used to fit other structures of interest.

The input properties of the oxides are the charge in the equilibrium bulk crystal, the electrostatic energy, the cohesive energy, the lattice constant, and the single-crystal elastic constants. With the metal EAM potential parameters (Table I) given, the remaining adjustable parameters are the four parameters χ, J, ξ, and Z for the charge properties of each of the three elements O, Al, and Zr, seven parameters r_e, α, β, A, B, κ, and λ for the pair potential between each of the three pairs O-O, O-Al, and O-Zr, three additional parameters f_e, Γ, and Ψ for the electron density of oxygen, and 10 parameters $F_{0,1}$, $F_{1,1}$, $F_{2,1}$, $F_{0,2}$, $F_{1,2}$, $F_{2,2}$, $F_{0,0}$, $F_{1,0}$, $F_{2,0}$, and $F_{3,0}$ that define the spline to the oxygen embedding energy. Note that $\rho_{e,i}$ ($i=Al_2O_3, ZrO_2$) is known for the given crystals once the electron density of oxygen is defined. One additional requirement is that the splined oxygen embedding energy be continuous and have smooth first derivatives at junctions.

Of the four charge parameters above, ξ characterizes the electron shell and defines the rate at which the electron density decays as the distance from the nucleus increases. A realistic value of ξ was determined by fitting the electron density distribution in the oxide crystal to that obtained from the *ab initio* calculation. The values of other charge parameters determine the equilibrium cation and anion charges in the bulk oxides, the electrostatic components of the cohesive energies, and the function forms of the charge versus lattice constant relation. These charge-related quantities, unfortunately, have traditionally not been well defined or determined. On the other hand, the precise determination of these quantities that are only used for the input of the CTIP model may not be necessary because all the measurable properties of oxides will be fitted to the integrated CTIP+EAM model. In the Streitz-Mintmire original CTIP model,[26] the Al charge in an equilibrium corundum Al_2O_3 was taken to be $2.900e$. This equilibrium charge is about 97% of the maximum aluminum charge of $3e$. It is also equivalent to an oxygen charge of $-1.933e$. While fitting of the charge parameters can be improved in the future when *ab initio* calculations or experiments provide better definition and data for charges, our tests indicated that the Streitz-Mintmire choice of the charges is reasonable and can produce realistic results within the context of the model. Hence, we assumed an equilibrium oxygen charge of $-1.933e$ in both Al_2O_3 and ZrO_2 bulk crystals. The electrostatic components of the cohesive energies of oxides were constrained in a range so that they must account for the extra cohesive energies of oxides with respect to those of pure metal and pure oxygen crystals. These electrostatic components were adjusted iteratively with EAM

TABLE III. CTIP parameters for O, Al, and Zr.

Element	$q_{\min}$	$q_{\max}$	χ (eV)	J (eV)	ξ (Å^{-1})	Z
O	−2	0	2.000	13.992	2.144	0.000
Al	0	3	−3.402	10.216	0.968	0.561
Zr	0	4	−3.360	7.954	0.816	0.641

TABLE IV. EAM parameters for O-O, O-Al, and O-Zr pair potentials.

Pair	r_e (Å)	α	β	A (eV)	B (eV)	κ	λ
O-O	3.315 171	5.716 137	3.758 299	0.263 795	0.273 569	0.498 438	0.560 282
O-Al	2.511 075	8.574 224	4.669 743	0.208 662	0.678 293	0.355 898	1.014 487
O-Zr	2.311 373	7.932 056	4.487 195	1.316 054	1.646 021	0.069 542	1.391 275

parameters so that the overall fitting was optimized. With these, the charge parameters of the three elements were determined and are listed in Table III, where the charge bounds, $q_{\min,i}$ and $q_{\max,i}$, are also listed for each element (i =O,Al,Zr).

For perfect oxides, analytical relationships between the charge parameters that give exactly the target equilibrium charges can be derived. By fitting to the bulk charge, a nonzero χ is obtained, When χ is not zero, isolated atoms will have a nonzero charge due to self-ionization. This can be seen from Eq. (B1) where a q of opposite sign with χ reduces the energy. The consequence of this is that the charge will not go to zero as the oxide crystal is expanded to infinity. To be consistent with the underlying assumption of our model that isolated atoms have zero charge, we have used a cutoff on χ. We assumed that χ takes the fitted value when the distance between any oxygen atom and a nearby atom is small. χ then diminishes towards zero as this distance approaches the cutoff distance of the potential. If χ_0 is the fitted value of χ, r is the distance between an oxygen atom and its nearby neighbor, r_s is the starting point for χ to vary, and r_c is the cutoff distance, a smooth approach to the χ cutoff can be achieved:

$$\chi = \frac{1}{2}\left[1+\cos\left(\frac{r-r_s}{r_c-r_s}\right)\pi\right]\chi_0 . \tag{14}$$

It should be pointed out that we provided Eq. (14) for the integrity of the model and applied it in our calculations. We did not find any serious problems without the inclusion of Eq. (14) in the simulations, as the Coulomb interaction is the dominant cause for the introduction of charge and the charge caused by self-ionization is small for the fitted parameter values used here.

The primary considerations during parametrization of the potential is to determine the remaining unknown parameters so that the potential best predicts the equilibrium lattice constant, cohesive energy, and elastic constants of the oxide systems (here the corundum Al_2O_3 and cubic ZrO_2 crystals). We have utilized the Rose universal equation[29] to assist with parameter fitting. The Rose crystal energy equation can be written

$$E_{\text{Rose}} = -E_c(1+a_s)\exp(-a_s), \tag{15}$$

TABLE V. EAM parameters for oxygen electron density.

f_e	Γ	Ψ
1.502 175	2.444 388	0.645 585

with

$$a_s = \varepsilon\sqrt{\frac{9B\Omega_0}{E_s}}, \tag{16}$$

where ε is the isotropic strain, B is the bulk modulus, E_c is the equilibrium cohesive energy, and Ω_0 is the equilibrium atomic volume. A convenient feature of the Rose equation is that at $\varepsilon=0$, it has an energy minimum E_c, and a second derivative that exactly predicts the bulk modulus B. Because of this, an exact fit of the cohesive energy, lattice constant, and bulk modulus for a cubic oxide can be simultaneously achieved if the following equation is strictly enforced:

$$E_t = E_{\text{es}} + E_n = E_{\text{Rose}} . \tag{17}$$

Notice that all the unknown parameters at this stage are contained in the expression for E_n. For fitting, all the parameters needed to define the oxygen electron density and the O-O and O-M (M denotes Al and Zr) pair potentials were first approximated by a best guess. This allows all the energy terms and their first and second derivatives in E_n to be calculated except for those related to oxygen embedding energy functions. The oxygen embedding energy and its first and second derivatives at the equilibrium electron density of the oxygen site in each oxide can then be solved from Eq. (17) as the oxygen embedding energy is the only unknown in the equation. Knowledge of these oxygen embedding energy values is sufficient to calculate all the elastic constants (we point out that while the position dependence of the charge does not affect forces and stresses as shown in Appendix B,

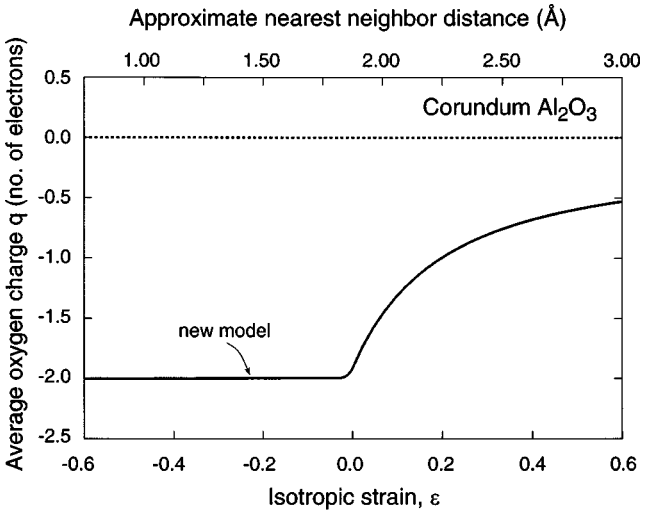

FIG. 3. Average anion charge of corundum Al_2O_3 as a function of isotropic strain predicted by our CTIP model.

TABLE VI. EAM parameters for the oxygen embedding energy spline function.

i	$F_{0,i}$	$F_{1,i}$	$F_{2,i}$	$F_{3,i}$	$\rho_{e,i}$	$\rho_{\min,i}$	$\rho_{\max,i}$
0	−1.514 833	−3.726 519	−2.911 951	−0.700 265	57.825 648	0	57.825 648
1	−1.945 745	−1.361 354	10.075 953		68.030 174	57.825 648	71.584 480
3	−1.965 159	0.883 740	7.620 277		75.138 786	71.584 480	∞

it does affect the elastic constants). The total squared deviation between predicted elastic constants and the target elastic constants was then calculated for all the independent elastic constants (C_{11}, C_{13}, C_{33}, C_{44}, and C_{12} for the hcp Al_2O_3, and C_{11}, C_{12}, and C_{44} for the cubic ZrO_2). The oxygen embedding energy and its first and second derivatives at the equilibrium electron density of the oxygen site in each oxide were then used in Eq. (12) to calculate the oxygen embedding energy and its derivatives at the spline junctions. The squared deviation of oxygen embedding energy and its derivatives at each junction were then added to the squared deviation of the elastic constants. To guarantee the correct lattice constants for noncubic structures (i.e., zero normal stresses in all coordinate directions), the squares of the three normal stresses were also included to obtain a total squared deviation. The conjugate graduate method as described in Appendix D was used to minimize the total squared deviation by adjusting the parameters needed to define the oxygen electron density and the O-O and O-M (M=Al and Zr) pair potentials. Once this was performed, the oxygen embedding energy values were used to define Eq. (12). Finally, Eq. (13) was defined under the condition that the function is zero at $\rho=0$ and is continuous with a continuous derivative at the right junction, $\rho=\rho_{\min,1}$. The fitted parameters deduced with this procedure are listed in Table IV for various pair interactions, Table V for oxygen electron density, and Table VI for oxygen embedding energy. Based upon this set of parameters, the predicted (unrelaxed) properties of the oxides are compared with their target values in Table VII. Here, the experimental lattice constants of Al_2O_3,[30] the experimental cohesive energies of Al_2O_3,[17,31] and ZrO_2 (see Appendix A), and experimental elastic constants of Al_2O_3 (Ref. 31) were used as the target values. The target values of the lattice constants and elastic constants of the cubic ZrO_2 were obtained using our *ab initio* calculations. It can be seen from Table VII that the predicted properties are in very good agreement with the target values.

VI. CHARACTERISTICS OF THE MODIFIED CTIP+EAM POTENTIAL

The modified CTIP+EAM potential is essentially equivalent to the existing EAM potential database[17] when used for pure metals. This EAM potential database has been well characterized and has been successfully applied to a variety of metal problems.[17,18] As a result, the several simulations performed here were all chosen to involve oxygen so that the application of the CTIP+EAM model in metal oxides can be characterized. For a given crystal, the calculated charges are determined only from the CTIP part of the potential and are independent of the EAM parameters. For a first test, the CTIP model as described above was used to calculate the charge as a function of isotropic lattice strain for the corundum phase of Al_2O_3 and the cubic phase of ZrO_2. During calculations, we used a ω coefficient of 10.0 for establishing charge bounds. Results for the anion charges of Al_2O_3 are plotted in Fig. 3. Similar results were obtained for ZrO_2. To test the charge stability, results were obtained for a wide

TABLE VII. Model predicted and target lattice constants a and c, cohesive energies E_c, and elastic constants C_{11}, C_{13}, C_{33}, C_{44}, C_{12}, C_{14}, and C_{66}.

		Al_2O_3		ZrO_2	
Physical property		Predicted	Target	Predicted	Target
Lattice constants (Å)	a	4.759	4.759	5.150	5.150
	c	12.991	12.991		
E_c (eV)		6.461	6.461	7.640	7.640
Elastic constants (eV/Å^3)	B	1.577	1.577	1.481	1.481
	C_{11}	3.452	3.108	3.158	3.181
	C_{13}	0.632	0.701	0.642	0.631
	C_{33}	3.259	3.119	3.158	3.181
	C_{44}	0.879	0.921	0.543	0.558
	C_{12}	0.750	1.025	0.642	0.631
	C_{14}	−0.161	−0.147	0.000	0.000
	C_{66}	1.351	1.042	0.543	0.558

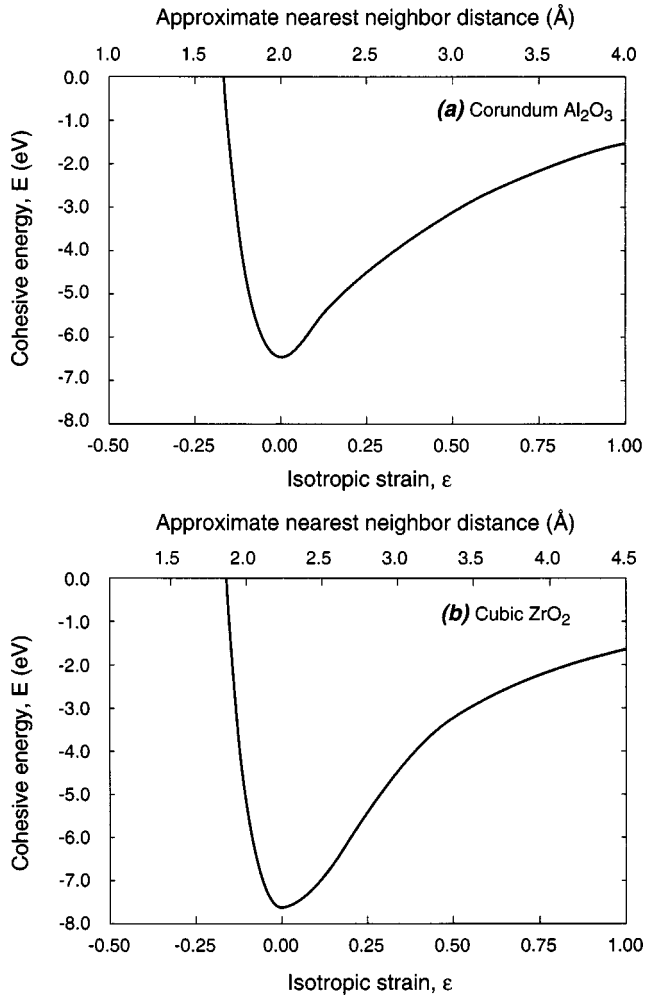

FIG. 4. Cohesive energies of (a) corundum Al_2O_3 and (b) cubic ZrO_2 as a function of isotropic strain (near equilibrium) predicted by our CTIP+EAM model.

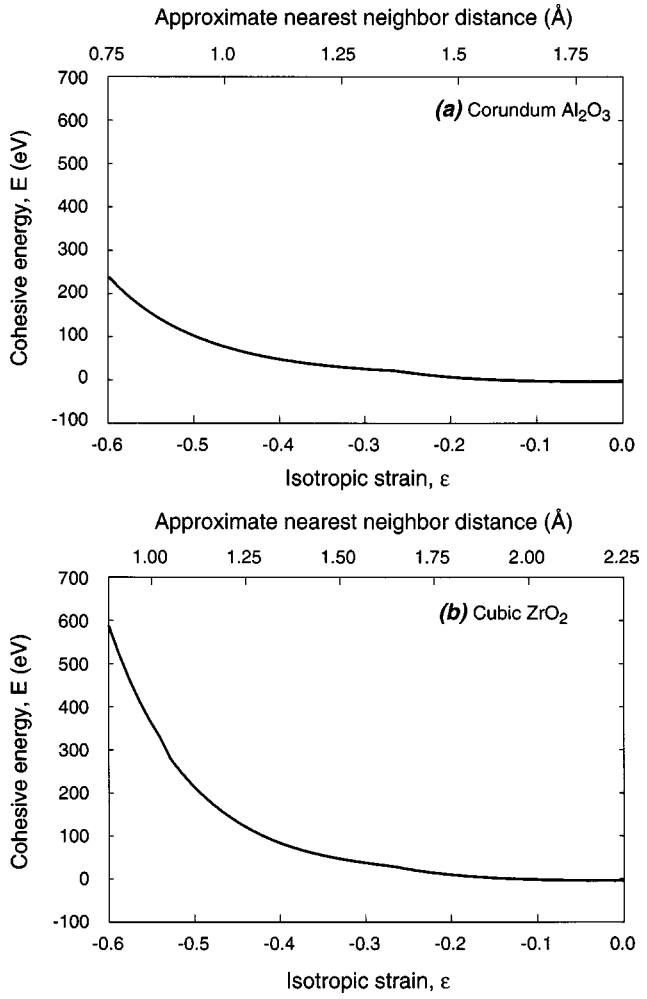

FIG. 5. Cohesive energies of (a) corundum Al_2O_3 and (b) cubic ZrO_2 as a function of isotropic strain (highly compressed) predicted by our CTIP+EAM model.

range of lattice strains from -0.6 to 0.6, which correspond to nearest-neighbor spacings from about 0.75 to 3.0 Å. Figure 3 indicates that the improved CTIP model predicts charge variation similar to the Streitz-Mintmire model[26] when the crystal lattice was stretched. On the other hand, it enables the oxygen charge to be bounded approximately to -2 as the lattice was compressed, demonstrating the successful implementation of the electron valence concept and elimination of the charge fluctuation problem.

The fitting procedures guarantee that the modified CTIP+EAM potential reproduces the Rose equation for the cohesive energy as a function of lattice constant in the vicinity of equilibrium bulk crystal for both corundum Al_2O_3 and cubic ZrO_2 structures. It is important to test that there is no instability when the crystal is highly compressed. For this, the cohesive energies of both the corundum Al_2O_3 and the cubic ZrO_2 were calculated for various isotropic strains from -0.5 to 1.0. The results are shown in Figs. 4(a) and 4(b), respectively, for Al_2O_3 and ZrO_2. The approximate nearest-neighbor distances are also included in the figures. Figures 4(a) and 4(b) indicate that the instability problem observed in Fig. 1 at small lattice constant is resolved by the improved CTIP+EAM model. Calculations were further extended to even lower strain ranges, and the results are shown in Fig. 5 with a greatly compressed ordinate scale. It can be seen that the stable calculations were achieved even at nearest-neighbor distance significantly smaller than 1.0 Å. Additional calculations for even more compressed crystals also did not indicate instability. We believe these results revealed sufficient stability for the application of this potential.

Since one of our intentions is to provide a potential that can be used in MD to simulate the growth ZrO_2 at high temperatures. When ZrO_2 is stabilized by Y_2O_3, ZrO_2 exhibits a tetragonal structure at high temperatures. However, the tetragonal ZrO_2 transforms into a cubic structure when the yttrium concentration is reduced. For pure ZrO_2, it is important to ensure that the cubic phase is most stable. To test this, both monoclinic and tetragonal ZrO_2 computational crystals were created according to the experimental crystal data.[30] The unrelaxed cohesive energies for both structures were lower (less stable) than that for the cubic structure. The derived CTIP+EAM potential was then used to relax the crystals. We found that the tetragonal structure relaxed to the cubic structure with a cohesive energy of 7.64 eV/atom. The

TABLE VIII. Surface energies (eV/Å^2) for various surfaces.

		Our CTIP+EAM model		Our *ab initio* model		Other *ab initio* models[a]	
Crystal	Surface	Unrelaxed	Relaxed	Unrelaxed	Relaxed	Unrelaxed	Relaxed
Al_2O_3	{0001}	0.37	0.25	0.22	0.09	0.24	0.11
	$\{10\bar{1}0\}$	0.37	0.31			0.22	0.09
	$\{10\bar{1}1\}$	0.36	0.31			0.23	0.16
	$\{11\bar{2}0\}$	0.32	0.28			0.16	0.12
	$\{10\bar{1}2\}$	0.38	0.32			0.16	0.12
ZrO_2	{110}	0.39	0.36	0.13	0.08	0.14	

[a]References 26, 32–34.

monoclinic nature of the monoclinic phase was reduced after relaxation. Its relaxed cohesive energy was 7.42 eV/atom, lower than that of a cubic structure. Since the cubic phase of ZrO_2 has the highest cohesive energy (we have fitted to this phase), the potential is therefore only applicable to simulations where the cubic ZrO_2 phase is expected to form (e.g., at high temperatures). It can also be used to simulate other phenomena such as self-diffusion and dislocation motion, in previously formed cubic ZrO_2 crystals. In its present form, the potential is not suited to simulate the growth of crystals under conditions where other ZrO_2 phases are preferred.

The surface energies predicted by the potential have also been explored. First, the effects of crystal thickness on surface energy was determined. A corundum Al_2O_3 crystal with $[\bar{1}100]$ *x* direction, [0001] *y* direction, and $[11\bar{2}0]$ *z* direction was used. Crystals with different thicknesses in the *y* direction were created. The equilibrium bulk crystal was obtained using periodic boundary conditions in all three coordinate directions with a flexible period length condition. The crystals with two equivalent Al-terminated {0001} surfaces were then created by using periodic boundary conditions in the *x* and *z* directions and a free boundary condition in the *y* direction. Both unrelaxed and relaxed surfaces were calculated. For relaxing the surfaces, the positions of atoms in the middle part of the crystals were fixed, and periodic lengths were not allowed to change. The surface energy was then calculated as the energy difference between the crystal with two *y* surfaces and the bulk crystal (scaled to have the same number of atoms) divided by the total area of the two surfaces. The results of the Al-terminated {0001} surface energy of Al_2O_3 indicated that the surface energy is almost independent of the crystal thickness beyond the thickness of 30 Å. As a result, crystals with a thickness (in *y* direction) of at least 30 Å were used for calculating various surface energies for both corundum Al_2O_3 and cubic ZrO_2 crystals. The results for relaxed and unrelaxed surface energies are listed in Table VIII.

For comparison, we selectively calculated some surface energies using *ab initio* methods. Manassidis and co-workers[32,33] also reported first-principles local-density functional calculations of surface energies of corundum Al_2O_3, and Christensen and Carter[34] published their *ab initio* calculations of unrelaxed {110} surface energy of cubic ZrO_2. These *ab initio* results are included in Table VIII.

The surface energies calculated by our CTIP+EAM model are higher than the *ab initio* results. The CTIP +EAM potential can be fitted to closely reproduce the *ab initio* surface energies as demonstrated by Streitz and Mintmire.[26] However, we noticed that ZrO_2 has a considerably larger cohesive energy than Al_2O_3 and yet our *ab initio* methods generally predicted very small unrelaxed and relaxed surface energies for ZrO_2. Accommodation of such a large discrepancy significantly affected the fitting of other properties. On the other hand, it is still an open debate as how well *ab initio* methods can be used to calculate surface energies in these systems. We also realized that all the crystals used in the *ab initio* calculations are less than 8 Å in thickness. This thickness is too short for ionic interactions. Manassidis and co-workers commented in their work that they expected the use of larger thicknesses may lead to substantially different surface energies. From these considerations, we did not specifically fit the surface energies during potential parametrization. This was found to result in much better fitting to the other properties.

CTIP+EAM potential calculations revealed a significant surface relaxation of the Al-terminated {0001} surface of the Al_2O_3 crystal. On this surface, the first surface monolayer is aluminum, the second monolayer is oxygen, the third and fourth monolayers are aluminum, and the subsequent monolayers are an alternative stacking of one oxygen and two aluminum layers. Simulations indicated that the outer Al monolayer was relaxed towards and became merged with the second (oxygen) layer. To test this result, the displacement of atoms near the surfaces (with respect to their bulk positions) was calculated using both CTIP+EAM molecular statics and *ab initio* energy minimization methods. The results are compared in Fig. 6, where the filled and unfilled circles represent CTIP+EAM and *ab initio* data, respectively. For the {0001} surface in the positive *y* direction, a positive displacement means that the plane moves out of the crystal while a negative displacement implies that the plane moves into the crystal. Figure 6 indicates that the CTIP+EAM generally match the relaxation pattern found in the *ab initio* calculations. They both indicate a strong relaxation of the outer Al surface into the bulk.

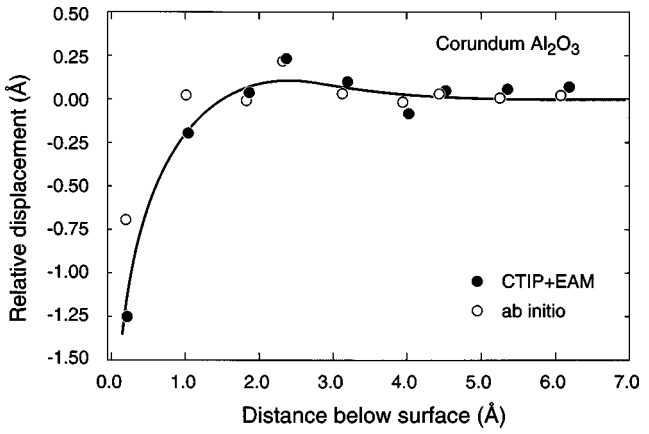

FIG. 6. Surface relaxation of the Al-terminated {0001} Al_2O_3 surface.

The calculations also yielded the charges on all of the ions. The anion and cation charges as a function of atom position from the Al-terminated {0001} surface of a corundum Al_2O_3 crystal are shown in Figs. 7(a) and 7(b). The anion and cation charges as a function of atom position from the O-terminated {111} surface of a cubic ZrO_2 crystal are shown in Figs. 7(c) and 7(d). The open and filled circles in the figures represent the relaxed and unrelaxed crystal data, respectively. It can be seen that the unrelaxed charge decreased as the free surface was approached. This agreed well with the original CTIP model[26] and physics of charge induction between cations and anions. The significant relaxation of the {0001} Al_2O_3 surface greatly reduced this effect. However, since little surface relaxation occurred on the {111} ZrO_2 surface, the charge on the {111} ZrO_2 surface remained much lower than that in the bulk after relaxation.

In heterostructure systems involving metals and oxygen, the electric field caused by charges can be effectively screened by any metallic clusters. A significant problem of any other type of empirical potentials is that they cannot physically implement this screening effect. One advantage of the CTIP model is that it naturally simulates such a screening effect by charge transfer. This is illustrated using a Zr/O multilayer. For simplicity, the Zr/O multilayer crystal is assumed to be simple cubic, with a lattice constant of 2.23 Å. The geometry of the crystal is shown in Fig. 8(a), where the bottom three monolayers are oxygen layers, and the top 17 monolayers are metallic zirconium layers. Using periodic boundary conditions in the x and z directions and a free boundary condition in the y direction, and by fixing the oxygen charge at $-2e$, the CTIP model was used to calculate the induced charge in the zirconium layers. The charge as a function of y coordinate (in units of monolayers) is shown in Fig. 8(b), where data for oxygen and zirconium are represented by filled and open circles, respectively, and the solid line is used to guide the eye.

It can be seen that positive charges are induced in the two zirconium monolayers closest to the negatively charged oxygen region, while charge on the other zirconium monolayers remains essentially zero. The existence of these charges can produce an electric field in the y direction. Using the assumption of point charges, the electric field at each ion's site (excluding the field produced by the ion itself) can be easily calculated. Figure 8(c) shows the electric field as a function of the y coordinate, where the filled and open circles now represent the electric field measured at the oxygen and zirconium sites, respectively, and the solid line is again used to

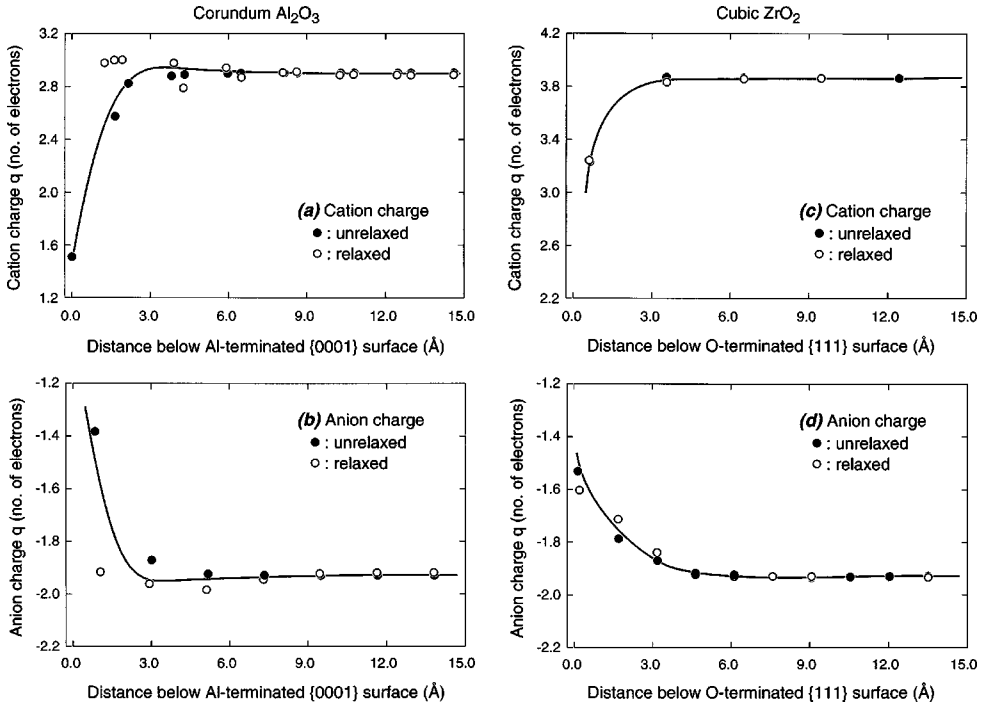

FIG. 7. Average (a) cation and (b) anion charges as a function of position along the [0001] thickness direction of the corundum Al_2O_3; and average (c) cation and (d) anion charges as a function of position along the [111] thickness direction of the cubic ZrO_2.

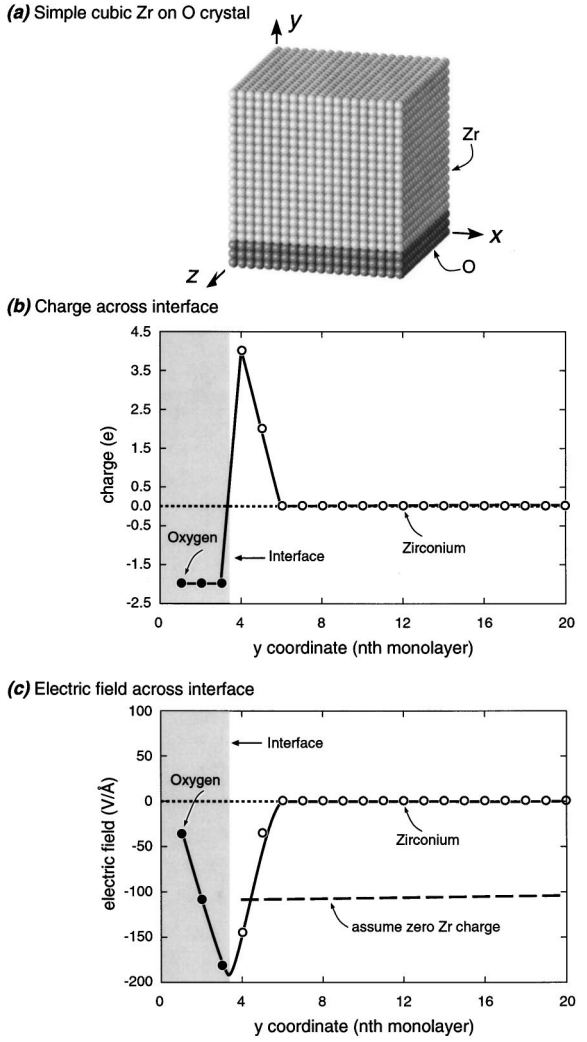

FIG. 8. Screen effect of our CTIP model. (a) a simple cubic (lattice constant 2.23 Å) Zr on O crystal; (b) the induced charge distribution in the Zr crystal when the O charge is fixed at $-2e$; and (c) the resulting electric field across the interface.

guide the eye. It can be seen that the electric field in the metal rapidly fell from -150 V/Å to almost 0 within three monolayers of the interface. For comparison, the electric field produced at the zirconium site by the oxygen layer alone (i.e., zero zirconium ion charge) is also shown as the dashed line. It is seen that the infinitely large plane of negatively charged oxygen produced an almost constant (y independent) electric field of about -100 V/Å. This result demonstrated that the CTIP model captures the metallic screening phenomenon, which is essential for valid simulations of metal-oxygen heterostructures.

An essential advantage for the modified CTIP+EAM model is that it predicts zero charges in any local metal alloy regions within metal/metal oxide mixtures. It should therefore be well suited for study of metal alloy oxidation. To test the validity of the potential for such simulations, the oxidation of a metal alloy containing two metal elements was explored. A disordered fcc $Al_{50}Zr_{50}$ alloy crystal with 36 $(22\bar{4})$ planes in the x direction, 15 (111) planes in the y

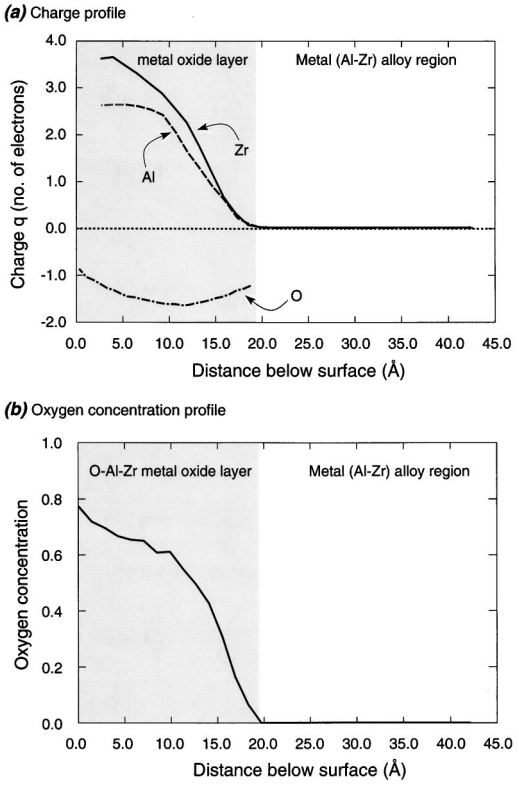

FIG. 9. (a) Average Al, Zr, and O charges and (b) oxygen concentration as a function of position along the [111] thickness direction of the oxidized $Al_{50}Zr_{50}$ alloy.

direction, and 10 $(2\bar{2}0)$ planes in the z direction was created. Using a free surface boundary condition in the y direction and periodic boundary conditions in the x and z directions, an oxygen atom vapor density of approximately 0.0003 atoms/Å^3 (about 10 atmospheric pressure) was introduced above the top y surface. A molecular dynamics simulation was then used to simulate oxidation of the surface at a temperature of 300 K. An abnormally high oxygen pressure was used to accelerate the oxidation. The charge was solved every 0.1 ps.

The simulation resulted in the formation of a ~20-Å-thick amorphous $Al_xZr_yO_z$ oxide layer on the $Al_{50}Zr_{50}$ alloy after 100 ps of oxidation. The average O, Al, and Zr charges as a function of depth in the $Al_{50}Zr_{50}$ alloy and its oxide are plotted in Fig. 9(a). The oxygen concentration profile through the oxide layer is shown in Fig. 9(b). It can be seen that the model predicted zero charge in the interior of the $Al_{50}Zr_{50}$ alloy. Towards the surface, the aluminum and zirconium charges rise until they approach their maximum values of $+3$ and $+4$, respectively. This corresponds well with the expected maximum oxygen concentration at the surface as shown in Fig. 9(b). The magnitude of the oxygen charge exhibits a maximum within the oxide bulk; it decreases as both the free surface and the metal/metal oxide interface are approached. The reduction of the oxygen charge at the surface is expected because the oxygen-rich surface region has an insufficient concentration of cations to ionize the oxygen atoms. The oxygen charge at the interface should also be low because the oxygen atoms are ionized by cations whose

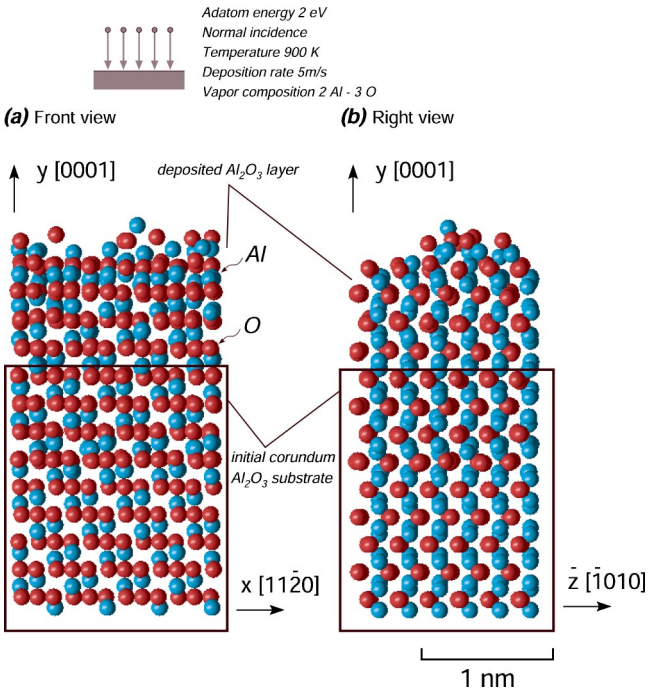

FIG. 10. (Color online) (a) Front and (b) right view of the vapor deposited Al_2O_3 film.

charges are low at the interface. These results provide good evidence that the CTIP+EAM model has captured much of the physics and chemistry needed to simulate the oxidation of metallic alloys.

Finally, we have used the CTIP+EAM potential in a preliminary simulation of the vapor phase growth of a corundum Al_2O_3 thin film. The basic approach was similar to that used for metal deposition.[17,18] The initial corundum crystal was created with a $[11\bar{2}0]$ x direction, a $[0001]$ y direction, and a $[10\bar{1}0]$ z direction. With periodic boundary conditions applied in x and z directions, the growth of the film in the y direction was simulated using an adatom energy 2.0 eV, an adatom's incidence perpendicular to the film surface, a deposition temperature of 900 K, a deposition rate of 5 nm/ns, and an exact aluminum oxygen atom vapor ratio of 2:3. The atomic structure obtained after 200 ps of deposition is shown in Fig. 10, where (a) and (b) correspond to the z and x views of the structure, respectively. Epitaxial growth of the crystalline Al_2O_3 film was found to have occurred. This is in good agreement with high-temperature vapor deposition experiments.[35] We believe that the potential has captured many of the important physical phenomena needed to realistically simulate the growth of metal/metal oxide heterostructures, though as with all empirical potentials, improvements are anticipated following more intensive applications.

VII. CONCLUSIONS

Simulations of structures involving both metals and their oxides require simultaneous treatment of metallic and ionic interactions. A charge transfer potential for ionic solids originally proposed by Streitz and Mintmire has been modified and coupled to a metal alloy embedded atom method potential to address such interactions. We found that by setting charge bounds upon each ion, the instability of the original CTIP potential can be removed. By setting metal charge bounds to a positive range and oxygen charge bounds to a negative range, the modified potential first allowed the CTIP model be used to analyze multimetal element problems. The charge bounds were implemented by a simple modification of the electrostatic energy. This modification of the energy has no effect if the charges are within the bounds. The new energy expression is numerically solvable using a computationally efficient conjugate gradient method. The proposed potential has been parameterized for the O-Al-Zr system by fitting to the bulk properties of the pure metals and their oxides. It describes well the cohesive energy and the ion charge as a function of lattice constants. It was also successfully used to predict surface relaxation and charge variations in various regions of a multilayer system including at free metal oxide surfaces, inside metal alloy bulk, inside metal oxide bulk, and at metal/metal oxide interfaces. The use of the potential in a molecular dynamics simulation of the vapor phase growth of a crystalline metal oxide film has also been demonstrated.

TABLE IX. Chemical reactions associated with oxide formation.

Chemical reactions	Heat of formation
$xM(\text{in crystal})+(y/2)O_2(\text{in gas})=M_xO_y$ (in crystal)	ΔH_1
$(y/2)O_2(\text{in gas})=y\text{O}(\text{in gas})$	$y\Delta H_2$
$xM(\text{in crystal})=xM(\text{in gas})$	$x\Delta H_3=xE_{c,M}$

ACKNOWLEDGMENT

We are grateful to the Office of Navy Research (S. Fisherman, Program Manager) for support of this work through grant N00014-01-1-0312.

APPENDIX A: COHESIVE ENERGY OF OXIDES

The handbook of thermochemical data usually lists the heat of formation (ΔH) of various chemical reactions. The heat of formation can be used to calculate cohesive energy of oxides. To derive the cohesive energy of an oxide M_xO_y, one needs to know the heat of formation for the chemical reactions given in Table IX. $E_{c,M}$ is the cohesive energy of metal. The cohesive energy of the oxide is then

$$E_{c,M_xO_y}=\Delta H_1-y\Delta H_2-x\Delta H_3. \tag{A1}$$

For ZrO_2, $\Delta H_1=-11.388$ eV,[36] $\Delta H_2=2.586$ eV,[31] $E_{c,\text{Zr}}=-6.36$ eV,[17] and hence $E_{c,ZrO_2}=-22.92$ eV/formula $=-7.64$ eV/atom.

APPENDIX B: PHYSICAL ORIGIN OF THE STREITZ-MINTMIRE CTIP MODEL

The ionization energy of an isolated ionizable atom, i, with a charge q_i can be expressed to second order as

$$E_i(q_i)=E_i(0)+\chi_i q_i+\tfrac{1}{2}J_i q_i^2, \tag{B1}$$

where χ_i is the electronegativity of atom i,[26] and J_i (>0) is referred to as an "atomic hardness" [37] or a self-Coulomb repulsion.[38] If N such ionizable atoms form an ionic crystal, the total electrostatic energy of the crystal is composed of both ionization energies and Coulomb energies resulting from interactions among the cations and anions. This total electrostatic energy can be written

$$E_{tes}=\sum_{i=1}^{N} E_i(q_i)+\tfrac{1}{2}\sum_{i=1}^{N}\sum_{j=i_1}^{i_N} V_{ij}(r_{ij},q_i,q_j). \tag{B2}$$

Here, $V_{ij}(r_{ij},q_i,q_j)$ is the Coulomb energy between atom i with a charge of q_i and atom j with a charge q_j, separated by a distance r_{ij}, and the notations i_1 and i_N represent the first and the last (Nth) neighbor of atom i. It should be pointed out that for simulations using long-range Coulomb interactions, it is often necessary to use cutoff distance that is much longer than the size of the periodic computational crystal cell. The neighbor list notation adopted here is concise because Eq. (B2) is valid for any cutoff distances as long as the neighbor list $i_1,\ldots,i_N$ covers all image atoms within the cutoff distance from atom i, including the images of i itself.

In the simplest case where all ions are point charges, the Coulomb energy in Eq. (B2) can be written

$$V_{ij}(r_{ij},q_i,q_j)=k_c\frac{q_i q_j}{r_{ij}}. \tag{B3}$$

Because the neighboring cations and anions have opposite sign charges in an ionic crystal, an increase of the magnitude of the charge may reduce the Coulomb energy. The tradeoff between an increase in ionization energy and a decrease in Coulomb energy can then define a set of equilibrium charges for all cations and anions that minimizes the total electrostatic energy. These equilibrium charges will vary depending upon the local environment. Replacing the fixed charges with the equilibrium charges deduced with a knowledge of the local environment overcomes many of the problems of fixed charge models and is the basis for the Streitz-Mintmire CTIP model.[26]

Point charges do not represent the electron distributions of ions well. It is more realistic to describe the charges in terms of an electron density distribution around an atom. Suppose that the charge q_i is partitioned into an electron density distribution function $\rho_i(\mathbf{r},q_i)$ around an atom i, where the position vector $\mathbf{r}$ emphasizes the spatial dependence rather than radial dependence. To simplify, spherically symmetric orbitals such as s orbitals can be assumed. $\rho_i(\mathbf{r},q_i)$ then becomes a radial function $\rho_i(r,q_i)$ where r can be simply viewed as the distance from the core of atom i. For this simple case, the electron density distribution function can be written

$$\rho_i(r,q_i)=Z_i\delta(r)+(q_i-Z_i)f_i(r), \tag{B4}$$

where $\delta(r)$ is a delta function [i.e., $\delta(r)=1$ at $r=0$ and $\delta(r)=0$ at $r\neq 0$], Z_i is an effective core charge (treated as a fitting parameter here), which should satisfy the condition $0<Z_i<N_i$, with N_i the total nuclear charge of the atom, and the function $f_i(r)$ describes the radial distribution of the valence charge in space that satisfies the condition that the volume integral of $f_i(r)$ over the entire space equals unity, i.e., $\int f_i(r)dV=1$. Note that q_i is partitioned into $\rho_i(r,q_i)$ because $\int \rho_i(r,q_i)dV=q_i$. It is pointed out that Eq. (B4) assumes rigid ions, and the shell model is ignored for simplicity. The main purpose is to develop a potential that can be used in MD simulations for random metal-oxygen mixtures. Such a simulation has not been possible with other potentials and we want to demonstrate that the CTIP model can achieve this using the simpler rigid ion case. Although the shell model is not used, we believe that it should have a negligible effect on the structure evolution during molecular dynamics simulations.[39] On the other hand, a more realistic shell model can be implemented by directly modifying Eq. (B4).[26]

With distributed charge, the electrostatic interaction $V_{ij}(r_{ij},q_i,q_j)$ must be integrated using

$$V_{ij}(r_{ij},q_i,q_j)=k_c\int\int\frac{\rho_i(r_i,q_i)\rho_j(r_j,q_j)}{r_{vv}}dV_i dV_j, \tag{B5}$$

where dV_i and dV_j are the two integrating volume units, r_i is the center distance between atom i and dV_i, r_j the center distance between atom j and dV_j, and r_{vv} the center distance between dV_i and dV_j. Note that an approximation is made because strictly, Eq. (B5) holds only for fixed charge distributions. Applying Eqs. (B4) and (B5), one can derive

$$\begin{aligned}V_{ij}(r_{ij},q_i,q_j)=&k_c q_i q_j[f_i|f_j]+k_c q_i Z_j([j|f_i]-[f_i|f_j])\\&+k_c q_j Z_i([i|f_j]-[f_i|f_j])+k_c Z_i Z_j\\&\times\left([f_i|f_j]-[i|f_j]-[j|f_i]+\frac{1}{r_{ij}}\right),\end{aligned} \tag{B6}$$

where notations $[a|f_b]$ and $[f_a|f_b]$ ($a=i,j$, $b=i,j$, $a\neq b$) denote the Coulomb interaction integrals:

$$[a|f_b]=\int\frac{f_b(r_b,q_b)}{r_{av}}dV_b, \tag{B7}$$

$$[f_a|f_b]=\int\int\frac{f_a(r_a,q_a)f_b(r_b,q_b)}{r_{vv}}dV_a dV_b. \tag{B8}$$

In general, the electron density is assumed to decrease with distance from the core of an atom. To capture the decay of $f_i(r)$ with r while maintaining mathematical simplicity, an exponential function for $f_i(r)$ was used:

$$f_i(r)=\frac{\xi_i^3}{\pi}\exp(-2\xi_i r), \tag{B9}$$

where the parameter ξ_i controls the spread of the electron distribution. Based upon Eqs. (B2) and (B6), the total electrostatic energy can be written as

$$E_{tes}=E_0+\sum_{i=1}^{N} q_i X_i+\tfrac{1}{2}\sum_{i=1}^{N}\sum_{j=1}^{N} q_i q_j V_{ij}, \qquad \text{(B10)}$$

where

$$E_0=\sum_{i=1}^{N} E_i(0)+\tfrac{1}{2}\sum_{i=1}^{N}\sum_{j=i_1}^{i_N} k_c Z_i Z_j \times\left([f_i|f_j]-[i|f_j]-[j|f_i]+\frac{1}{r_{ij}}\right), \qquad \text{(B11)}$$

$$X_i=\chi_i+\sum_{j=i_1}^{i_N} k_c Z_j([j|f_i]-[f_i|f_j]), \qquad \text{(B12)}$$

$$V_{ij}=J_i\delta_{ij}+\sum_{k=j(i_1)}^{j(i_N)} k_c[f_i|f_k]. \qquad \text{(B13)}$$

In Eq. (B13), $\delta_{ij}=1$ when $i=j$ and $\delta_{ij}=0$ when $i\neq j$, and the summation indexes $j(i_1)$ and $j(i_N)$ means that the summation is over all the j atoms (i.e., atom j and all its images) that are i's neighbors. Note that E_0 in Eq. (B10) is independent of charge q. Such a potential term can be absorbed into the nonelectrostatic energy and hence can be ignored here. We can then define a normalized electrostatic energy E_{es} that has the required zero value when all the charges are zero:

$$E_{es}=E_1-E_0=\sum_{i=1}^{N} q_i X_i+\tfrac{1}{2}\sum_{i=1}^{N}\sum_{j=1}^{N} q_i q_j V_{ij}. \qquad \text{(B14)}$$

In Eq. (B14), X_i and V_{ij} can be calculated using Eqs. (B12) and (B13) for a given crystal configuration if the potential parameters ξ_i, Z_i, χ_i and J_i are given. Equation (B14) is then a quadratic function with respect to q_i ($i=1,...,N$). Under the condition that the system is neutral, $\Sigma_{i=1}^{N} q_i=0$, E_{es} becomes a function of $N-1$ independent variables q_i ($i=1,...,N-1$). Setting the derivatives of E_{es} with respect to these $N-1$ independent variables to zero is equivalent to setting equal values for the derivatives of E_{es} with respect to the N dependent variables (i.e., $\mu_i=\partial E_{es}/\partial q_i=\mu$, $i=1,...,N$). This leads to N linear equations for solving equilibrium charges that give the minimum energy:

$$\sum_{j=1}^{N} V_{ij}q_j=\mu-\chi_i, \quad i=1,2,...,N. \qquad \text{(B15)}$$

If V_{ij}^{-1} is the matrix inverse of V_{ij}, q_i can be solved as

$$q_i=\sum_{j=1}^{N} V_{ij}^{-1}(\mu-\chi_j). \qquad \text{(B16)}$$

q_i can be determined if μ is known. Using the system neutral condition $\Sigma_{i=1}^{N} q_i=0$, μ in fact can be calculated as

$$\mu=\left(\sum_{i=1}^{N}\sum_{j=1}^{N} V_{ij}^{-1}\chi_j\right)\Big/\left(\sum_{i=1}^{N}\sum_{j=1}^{N} V_{ij}^{-1}\right). \qquad \text{(B17)}$$

Once the charge is solved, Eq. (B14) can be used to calculate the electrostatic interaction between atoms. A feature of the CTIP model that is useful for implementing it within a MD code is that while the charge generally changes as the atom moves, this position dependence of charge does not affect the calculations of forces and stresses. For instance, the x component of the force on an atom i due to the position dependence of q can be expressed as

$$f_{x,i}|^q=-\left.\frac{\partial E_{es}}{\partial x}\right|^q=-\sum_{i=1}^{N}\frac{\partial E_{es}}{\partial q_i}\frac{\partial q_i}{\partial x}. \qquad \text{(B18)}$$

Because charges are obtained from equilibrium conditions $\partial E_{es}/\partial q_i=\mu_i=\mu$, and the system is neutral, $\Sigma_{i=1}^{N} q_i=0$, Eq. (B18) becomes

$$f_{x,i}|^q=-\mu\sum_{i=1}^{N}\frac{\partial q_i}{\partial x}=0. \qquad \text{(B19)}$$

APPENDIX C: EWALD SUMMATION

Coulomb interactions are long-range interactions that decay with $1/r_{ij}$. For an ionic crystal that is periodically stacked to infinity, a direct sum of this kind of long-range potentials,

$$S=\tfrac{1}{2}\sum_{i=1}^{N}\sum_{j=i_1}^{i_N}\frac{1}{r_{ij}},$$

imposes a serious divergent problem. Using the Zr-O potentials,[24] for instance, one can easily show that the lattice energy of ZrO_2 based upon the direct sum of the Coulomb energy oscillates between positive and negative values with a cutoff distance. There are a number of approaches to resolve this problem. One commonly used approach is the Ewald summation[40,41] technique.

In the Ewald summation method, an error function erf(x) and its complimentary function erfc(x)=1−erf(x) were used to decompose the Coulomb summation into two parts:

$$S=\tfrac{1}{2}\sum_{i=1}^{N}\sum_{j=i_1}^{i_N}\frac{q_i q_j}{r_{ij}}=\tfrac{1}{2}\sum_{i=1}^{N}\sum_{j=i_1}^{i_N}\frac{\mathrm{erfc}(\tau r_{ij})q_i q_j}{r_{ij}} +\tfrac{1}{2}\sum_{i=1}^{N}\sum_{j=i_1}^{i_N}\frac{\mathrm{erf}(\tau r_{ij})q_i q_j}{r_{ij}}. \qquad \text{(C1)}$$

One useful feature of erfc(x) is that it decreases rapidly with x. By choosing the proper convergent coefficient τ, erfc(τr_{ij})/r_{ij} can be made negligibly small at large r_{ij}. This short-range interaction can then be directly summed up. The term erf(τr_{ij})/r_{ij} is small at short distances, but cannot be neglected at large distances. However, if the computational cell has periodic boundary conditions in all the three coordinate dimensions, a Fourier transform can be applied to convert the periodic summation

$$\tfrac{1}{2}\sum_{i=1}^{N}\sum_{j=i_1}^{i_N}\frac{\mathrm{erf}(\tau r_{ij})q_i q_j}{r_{ij}}$$

in normal space to a summation in reciprocal space:

$$\frac{1}{2}\sum_{i=1}^{N}\sum_{j=i_1}^{i_N}\frac{\mathrm{erf}(\tau r_{ij})q_iq_j}{r_{ij}} = -\frac{\tau}{\sqrt{\pi}}\sum_{i=1}^{N}q_i^2+\frac{2\pi}{V}\sum_{i=1}^{N}\sum_{j=1}^{N}q_iq_j \times \sum_{\substack{l,m,n \\ !(l=m=n=0)}}\frac{\exp(-R^2/4\tau^2)\mathrm{Re}[\exp(\sqrt{-1}\vec{R}\cdot\vec{r}_{ij})]}{R^2}, \tag{C2}$$

where ! excludes the condition specified in ( ), $V=L_xL_yL_z$ is the volume of the periodic cell, L_x, L_y, and L_z are the lengths of the cell in the x, y, and z directions,

$$\vec{R}=2\pi\left(\frac{l}{L_x}\vec{x}+\frac{m}{L_y}\vec{y}+\frac{n}{L_z}\vec{z}\right)$$

is a reciprocal-lattice vector, $\vec{r}_{ij}=(x_j-x_i)\vec{x}+(y_j-y_i)\vec{y}+(z_j-z_i)\vec{z}$ is the vector between atom i and j in the normal space, R is the norm of $\vec{R}$, Re( ) takes the real part of the complex number, and $\vec{x}$, $\vec{y}$, and $\vec{z}$ are unit vectors in the three coordinate directions. The convergence in the reciprocal space can also be made fast by the proper choice of τ. Therefore, Eqs. (C1) and (C2) can be used for atomistic simulations for three dimensional ionic atomic assembly.[40]

The computational cell is two-dimensional for surface problems. If the two-dimensional cell is in the x-z plane, then it will lose the periodicity in the y direction. Equation (C2), which is based upon periodic boundary conditions in all three directions, cannot be used then. One can imagine, however, that a three-dimensional space is occupied by equally separated sheets of two-dimensional crystals of the same thickness. If we allow the y dimension of our computational cell to be exactly one sheet thickness plus the sheet spacing, then the periodic boundary condition holds even in the y direction for these equally separated sheets. Equation (C2) can be used for this case. If we further imagine that the spacing between sheets is increased to infinity while the sheet thickness is kept constant, then we virtually simulate an isolated two dimensional slab.

One can decompose $\vec{R}$ into out-of-plane component $\vec{R}_y$ and in-plane component $\vec{R}_p$, $\vec{r}_{ij}$ into out-of-plane component $\vec{r}_{y,ij}$ and in-plane component $\vec{r}_{p,ij}$. To adapt Eq. (C2) for the two-dimensional case, the computational cell size in the y direction is assumed to be c. The volume of the unit cell is $V=cA$, with A being the area of the two-dimensional cell. Based on these notations, Eq. (C2) becomes:

$$\frac{1}{2}\sum_{i=1}^{N}\sum_{j=i_1}^{i_N}\frac{\mathrm{erf}(\tau r_{ij})q_iq_j}{r_{ij}} = -\frac{\tau}{\sqrt{\pi}}\sum_{i=1}^{N}q_i^2+\sum_{i=1}^{N}\sum_{j=1}^{N}q_iq_j\sum_{m=-\infty}^{\infty}\mathrm{Re}\left\{\frac{2\pi}{Ac}\sum_{\substack{l,n \\ !(l=m=n=0)}}\exp\left(-\frac{R_p^2}{4\tau^2}\right)\exp(\sqrt{-1}\vec{R}_p\cdot\vec{r}_{p,ij}) \times\frac{\exp\left(-\frac{R_y^2}{4\tau^2}\right)\exp(\sqrt{-1}R_yr_{y,ij})}{R_y^2+R_p^2}\right\}. \tag{C3}$$

Since $R_y(m)=2\pi(m/c)$, $dR_y=dR_y(m)-dR_y(m-1)=2\pi/c\to 0$ as $c\to 0$. The summation over m can be replaced by integral, and Eq. (C3) becomes

$$\frac{1}{2}\sum_{i=1}^{N}\sum_{j=i_1}^{i_N}\frac{\mathrm{erf}(\tau r_{ij})q_iq_j}{r_{ij}} = -\frac{\tau}{\sqrt{\pi}}\sum_{i=1}^{N}q_i^2+\sum_{i=1}^{N}\sum_{j=1}^{N}q_iq_j\,\mathrm{Re}\left\{\frac{1}{A}\sum_{l,n}\exp\left(-\frac{R_p^2}{4\tau^2}\right)\exp(\sqrt{-1}\vec{R}_p\cdot\vec{r}_{p,ij}) \times\int_{-\infty}^{\infty}\frac{\exp(-R_y^2/4\tau^2)\exp(\sqrt{-1}R_yr_{y,ij})}{R_y^2+R_p^2}dR_y\right\}. \tag{C4}$$

Notice that in Eq. (C4) the condition $!(m=n=1=0)$ in the summation has been removed. This is valid in the summation of Coulomb interactions where the system is neutral $\Sigma_{i=1}^{N}q_i=0$. The integral in Eq. (C4) can be solved to yield

$$\frac{1}{2}\sum_{i=1}^{N}\sum_{j=i_1}^{i_N}\frac{\mathrm{erf}(\tau r_{ij})q_iq_j}{r_{ij}} = -\frac{\tau}{\sqrt{\pi}}\sum_{i=1}^{N}q_i^2+\frac{\pi}{2A}\sum_{i=1}^{N}q_i\sum_{j=1}^{N}q_j\left\{-2\left(r_{y,ij}[1-\mathrm{erfc}(\tau r_{y,ij})]+\frac{\exp(-\tau^2r_{y,ij}^2)}{\sqrt{\pi}\tau}\right) + \sum_{\substack{l,n \\ !(l=n=0)}}\frac{\exp(R_yr_{y,ij})\mathrm{erfc}(R_y/2\tau+\tau r_{y,ij})+\exp(-R_yr_{y,ij})\mathrm{erfc}(R_y/2\tau-\tau r_{y,ij})}{R_y}\cos(\vec{R}_y\cdot\vec{r}_{y,ij})\right\}. \tag{C5}$$

Equation (C5) can be used for Ewald summation for two-dimensional crystals.[41]

APPENDIX D: CONJUGATE GRADIENT METHOD

For a function F with N independent variables x_i $(i=1,2,...,N)$, the function can be efficiently minimized using the conjugate gradient method.[42] The method contains the following iteration procedures:

(1) Starting from initial guessed variables, say $x_{i,0}=0$, F was first minimized along the steepest descent direction $d_{i,0}=g_{i,0}=-\partial F/\partial x_{i,0}$, $i=1,2,...,N$. This results in new variables $x_{i,1}=x_{i,0}+\sigma_0 d_{i,0}$, where σ_0 is the march distance along the search direction and can be obtained from $\partial F/\partial\sigma_0=0$. In some cases, such as Eq. (B14) where $\partial E_{es}(\sigma_0)/\partial\sigma_0$ is a linear function of σ_0, σ_0 can be directly solved. For other cases, such as Eq. (9) where $\partial E_{es}(\sigma_0)/\partial\sigma_0$ can only be calculated locally as it contains nonconstant prefactors, σ_0 cannot be solved in a closed form. A general function, such as Eq. (9), however, can be solved with many standard iteration algorithms. We used the Newton-Raphson method[43] to solve for σ_0.

(2) The search direction for the next and the subsequent iterations $(k=2,3,...)$ was obtained using the relation

$$d_{i,k}=g_{i,k}+\frac{\sum_{i=1}^{N} g_{i,k}}{\sum_{i=1}^{N} g_{i,k-1}} d_{i,k-1}, \tag{D1}$$

where $g_{i,k}=-\partial F/\partial x_{i,k}$.

(3) The new iteration was obtained as $x_{i,k+1}=x_{i,k}+\sigma_k d_{i,k}$, with σ_k solved from $\partial F/\partial\sigma_k=0$. The iteration is continued until the updates are sufficiently small.

APPENDIX E: ALLOY EMBEDDED ATOM METHOD MODEL

Using the EAM, the nonelectrostatic energy can be expressed as[16]

$$E_n=\tfrac{1}{2}\sum_{i=1}^{N}\sum_{j=i_1}^{i_N}\phi_{ij}(r_{ij})+\sum_{i=1}^{N}F_i(\rho_i), \tag{E1}$$

where $\phi_{ij}(r_{ij})$ represents the pair energy between atoms i and j separated by r_{ij}, and F_i stands for the embedding energy to embed an atom i into a local site with electron density ρ_i. ρ_i can be calculated using

$$\rho_i=\sum_{j=i_1}^{i_N} f_j(r_{ij}), \tag{E2}$$

with $f_j(r_{ij})$ the electron density at the site of atom i arising from atom j at a distance r_{ij} away.

It has been demonstrated that for elemental systems, the representation of a given potential using the EAM format described in Eq. (E1) is not unique.[44] This arbitrary representation of elemental potentials, however, would change alloy properties when elemental potentials are used for alloys. The potential cutoff distances fitted for individual elements are also not necessarily consistent. Because of these, the EAM potentials developed for atoms of a single element generally cannot be applied to alloys. While alloys can still be studied by fitting individual alloy potentials separately, the alloys that can be explored are greatly limited. By normalizing the EAM potentials and introducing an EAM alloy model,[44] a generalized EAM database[17] where alloy potentials can be constructed from elemental potentials without any more fitting has been developed. In the EAM database, the generalized elemental pair potentials are written:

$$\phi(r)=\frac{A\exp\left[-\alpha\left(\frac{r}{r_e}-1\right)\right]}{1+\left(\frac{r}{r_e}-\kappa\right)^{20}}-\frac{B\exp\left[-\beta\left(\frac{r}{r_e}-1\right)\right]}{1+\left(\frac{r}{r_e}-\lambda\right)^{20}}, \tag{E3}$$

where r_e is the equilibrium spacing between nearest neighbors, A,B,α,β are four adjustable parameters. Notice that the denominators introduced in Eq. (E3) equal to 1 when r is small, but go to infinity as r increases. This provides a natural cutoff for the potential and the additional two parameters κ, λ control how fast the potential is cutoff.

The electron density function is taken with the same form as the attractive term in the pair potential with the same values of β, and λ, i.e.,

$$f(r)=\frac{f_e\exp\left[-\beta\left(\frac{r}{r_e}-1\right)\right]}{1+\left(\frac{r}{r_e}-\lambda\right)^{20}}. \tag{E4}$$

To have embedding energy functions that can work well over a wide range of electron density, three equations are used to separately fit to different electron density ranges. For a smooth variation of the embedding energy, these equations are required to match values and slopes at their junctions. These equations are listed in the following:

$$F(\rho)=\sum_{i=0}^{3}F_{ni}\left(\frac{\rho}{\rho_n}-1\right)^i,\quad \rho<\rho_n,\quad \rho_n=0.85\rho_e, \tag{E5}$$

$$F(\rho)=\sum_{i=0}^{3}F_{i}\left(\frac{\rho}{\rho_e}-1\right)^i,\quad \rho_n\leqslant\rho<\rho_0,\quad \rho_0=1.15\rho_e, \tag{E6}$$

$$F(\rho)=F_e\left[1-\ln\left(\frac{\rho}{\rho_s}\right)^{\eta}\right]\left(\frac{\rho}{\rho_s}\right)^{\eta},\quad \rho_0\leqslant\rho. \tag{E7}$$

Note that Eq. (E7) has been modified from Ref. 17 (ρ_e is replaced by a new parameter ρ_s) to better describe the metal properties. Equations (E3)–(E7) sufficiently define the potentials for elemental metals. For metal alloy calculations, one also needs cross pair potentials between different species a and b. According to the alloy EAM model,[44] the pair potential between different species a and b can be written

$$\phi_{ab}(r)=\frac{1}{2}\left(\frac{f_b(r)}{f_a(r)}\phi_{aa}(r)+\frac{f_a(r)}{f_b(r)}\phi_{bb}\right). \quad \text{(E8)}$$

To normalize all elemental potentials, the embedding energy and the elemental pair potentials are required to separately satisfy equilibrium (i.e., the functions are minimum at the equilibrium lattice structures). In summary, one needs 20 parameters for each element, r_e, f_e, ρ_e, ρ_s, α, β, A, B, κ, λ, F_{n0}, F_{n1}, F_{n2}, F_{n3}, F_0, F_1, F_2, F_3, η, F_e, to fully define the elemental and alloy metal potentials. These parameters have been published for 16 metals (Cu, Ag, Au, Ni, Pd, Pt, Al, Pb, Fe, Mo, Ta, W, Mg, Co, Ti, and Zr).[17]

*Author to whom correspondence should be addressed. Electronic address: xz8n@virginia.edu

[1] S. Virtanen, H. Wojtas, P. Schmuki, and H. Bohni, J. Electrochem. Soc. **140**, 2786 (1993).
[2] L. N. Satapathy, Mater. Res. Bull. **34**, 1233 (1999).
[3] S. B. Bhaduri and F. H. Froes, JOM **43**, 16 (1991).
[4] N. P. Padture, M. Gell, and E. H. Jordan, Science **296**, 280 (2002).
[5] G. Q. Lo, J. Ahn, and D. L. Kwong, IEEE Electron Device Lett. **13**, 457 (1992).
[6] M. Tondra, J. M. Daughton, D. Wang, R. S. Beech, A. Fink, and J. A. Taylor, J. Appl. Phys. **83**, 6688 (1998).
[7] G. A. Prinz, Science **282**, 1660 (1998).
[8] R. Nakatani and M. Kitada, J. Mater. Sci. Lett. **10**, 827 (1991).
[9] J. S. Moodera, L. R. Kinder, T. M. Wong, and R. Meservey, Phys. Rev. Lett. **74**, 3273 (1995).
[10] R. S. Beech, J. Anderson, J. Daughton, B. A. Everitt, and D. Wang, IEEE Trans. Magn. **32**, 4713 (1996).
[11] J. S. Moodera, J. Nassar, and G. Mahon, Annu. Rev. Mater. Sci. **29**, 381 (1999).
[12] Y. Matsumoto, M. Murakami, T. Shono, T. Hasegawa, T. Fukumura, M. Kawasaki, P. Ahmet, T. Chikyow, S. Koshihara, and H. Koinuma, Science **291**, 854 (2001).
[13] S. A. Wolf, D. D. Awschalom, R. A. Buhrman, J. M. Daughton, S. von Molnar, M. L. Roukes, A. Y. Chtchelkanova, and D. M. Treger, Science **294**, 1488 (2001).
[14] C. L. Liu, J. M. Cohen, J. B. Adams, and A. F. Voter, Surf. Sci. **253**, 334 (1991).
[15] H. Huang, G. H. Gilmer, and T. D. de la Rubia, J. Appl. Phys. **84**, 3636 (1998).
[16] M. S. Daw and M. I. Baskes, Phys. Rev. B **29**, 6443 (1984).
[17] X. W. Zhou, H. N. G. Wadley, R. A. Johnson, D. J. Larson, N. Tabat, A. Cerezo, A. K. Petford-Long, G. D. W. Smith, P. H. Clifton, R. L. Martens, and T. F. Kelly, Acta Mater. **49**, 4005 (2001).
[18] W. Zou, H. N. G. Wadley, X. W. Zhou, and R. A. Johnson, Phys. Rev. B **64**, 174418 (2001).
[19] M. Baudin and K. Hermansson, Surf. Sci. **474**, 107 (2001).
[20] B. G. Dick and A. W. Overhauser, Phys. Rev. **112**, 90 (1958).
[21] A. Dwivedi and A. N. Cormack, Philos. Mag. A **61**, 1 (1990).
[22] P. J. D. Lindan and M. J. Gillan, J. Phys.: Condens. Matter **5**, 1019 (1993).
[23] G. V. Lewis and C. R. A. Catlow, J. Phys. C **18**, 1149 (1985).
[24] M. S. Khan, M. S. Islam, and D. R. Bates, J. Mater. Chem. **8**, 2299 (1998).
[25] C. R. A. Catlow, J. Chem. Soc. Faraday Trans. **86**, 1167 (1990).
[26] F. H. Streitz and J. W. Mintmire, Phys. Rev. B **50**, 11996 (1994).
[27] T. Campbell, R. K. Kalia, A. Nakano, P. Vashishta, S. Ogata, and S. Rodgers, Phys. Rev. Lett. **82**, 4866 (1999).
[28] S. Ogata and T. J. Campbell, J. Phys.: Condens. Matter **10**, 11449 (1998).
[29] J. H. Rose, J. R. Smith, F. Guinea, and J. Ferrante, Phys. Rev. B **29**, 2963 (1984).
[30] *Crystal Data, Determinative Tables*, 3rd ed., Vol. II: *Inorganic Compounds*, edited by J. D. H. Donnay *et al.* (JCPDS - International Center for Diffraction Data, Swarthmore, Pennsylvania, 1973).
[31] *CRC Handbook of Chemistry and Physics* (CRC Press, Boca Raton, 1978).
[32] I. Manassidis, A. DeVita, and M. J. Gillan, Surf. Sci. Lett. **285**, L517 (1993).
[33] I. Manassidis and M. J. Gillan, J. Am. Ceram. Soc. **77**, 335 (1994).
[34] A. Christensen and E. A. Carter, Phys. Rev. B **58**, 8050 (1998).
[35] Z. Chen and M. C. Jin, J. Mater. Sci. Lett. **11**, 1023 (1992).
[36] I. Barin, *Thermochemical Data of Pure Substances* (VCH, Cambridge, 1989).
[37] R. G. Parr and R. G. Pearson, J. Am. Chem. Soc. **105**, 7512 (1983).
[38] A. K. Rappe and W. A. Goddard, J. Phys. C **95**, 3358 (1991).
[39] P. J. D. Lindan and M. J. Gillan, J. Phys.: Condens. Matter **5**, 1019 (1993).
[40] D. E. Parry, Surf. Sci. **49**, 433 (1975).
[41] D. M. Heyes, Surf. Sci. Lett. **293**, L857 (1993).
[42] R. Fletcher and C. M. Reeves, Computer J. (UK) **7**, 149 (1964).
[43] W. H. Press, B. P. Flannery, S. A. Teukolsky, and W. T. Vetterling, *Numerical Recipes, the Art of Scientific Computing (Fortran Version)* (Cambridge University Press, Cambridge, 1989), p. 254.
[44] R. A. Johnson, Phys. Rev. B **39**, 12554 (1989).